

This is a self-archived version of an original article. This version may differ from the original in pagination and typographic details.

Author(s): Schenke, B.; Schlichting, S.; Singh, P.

Title: Rapidity dependence of initial state geometry and momentum correlations in p+Pb collisions

Year: 2022

Version: Published version

Copyright: © 2022 American Physical Society

Rights: In Copyright

Rights url: <http://rightsstatements.org/page/InC/1.0/?language=en>

Please cite the original version:

Schenke, B., Schlichting, S., & Singh, P. (2022). Rapidity dependence of initial state geometry and momentum correlations in p+Pb collisions. *Physical Review D*, 105(9), Article 094023.
<https://doi.org/10.1103/PhysRevD.105.094023>

Rapidity dependence of initial state geometry and momentum correlations in p + Pb collisions

B. Schenke,¹ S. Schlichting²,,² and P. Singh^{2,3,4,*}

¹*Physics Department, Brookhaven National Laboratory, Building 510A, Upton, New York 11973, USA*

²*Fakultät für Physik, Universität Bielefeld, D-33615 Bielefeld, Germany*

³*Department of Physics, University of Jyväskylä, P.O. Box 35, Jyväskylä 40014, Finland*

⁴*Helsinki Institute of Physics, University of Helsinki, P.O. Box 64, Helsinki FI-00014, Finland*



(Received 19 February 2022; accepted 28 April 2022; published 20 May 2022)

Event geometry and initial state correlations have been invoked as possible explanations of long-range azimuthal correlations observed in high-multiplicity p + p and p + Pb collisions. We study the rapidity dependence of initial state momentum correlations and event-by-event geometry in $\sqrt{s} = 5.02$ TeV p + Pb collisions within the 3 + 1D IP-Glasma model [B. Schenke and S. Schlichting, *Phys. Rev. C* **94**, 044907 (2016)], where the longitudinal structure is governed by Jalilian-Marian-Iancu-McLerran-Weigert-Leonidov-Kovner rapidity evolution of the incoming nuclear gluon distributions. We find that the event geometry is correlated across large rapidity intervals whereas initial state momentum correlations are relatively short-range in rapidity. Based on our results, we discuss implications for the relevance of both effects in explaining the origin of collective phenomena in small systems.

DOI: [10.1103/PhysRevD.105.094023](https://doi.org/10.1103/PhysRevD.105.094023)

I. INTRODUCTION

The collective behavior observed in heavy ion collisions has led to the discovery of quark gluon plasma (QGP) and established the behavior of QGP as a nearly perfect fluid. The main observables associated with this collectivity are the anisotropic flow coefficients v_n , which characterize the anisotropies in the transverse momentum distributions of produced particles. Experimental measurements of these coefficients can be described extremely well using relativistic hydrodynamic simulations of heavy ion collisions [1–5]. Within the hydrodynamic picture, the final state momentum distributions are explained entirely via the response to the initial state geometry in the transverse (to the beam line) plane. Gradients of the pressure drive the directionally dependent expansion of the system, thus leaving an imprint of the initial shape of the fireball in the final particle spectra.

More recently, signals similar to those in heavy collisions have been found in the produced particle spectra of small collision systems, including p/d/³He + A and even p + p [6–11] and ultraperipheral Pb + Pb [12] collisions. Such findings have led to increased research regarding the question of how hydrodynamics could possibly be applicable in very small systems that produce only on the order of ten charged hadrons per unit rapidity (see [13] for a review), as well as on the exploration of alternative mechanisms that could generate the observed anisotropies

without requiring the creation of a nearly perfect fluid. Examples of the latter include kinetic theory [14–22], as well as the correlated (multi)particle production in the color glass condensate framework [23–40], where anisotropic momentum distributions result from correlations in the gluon distributions of the incoming nuclei.

While calculations involving final state effects (e.g., in the hydrodynamic framework) have been rather successful in describing the main features of the momentum anisotropies observed in small collision systems at RHIC and LHC [41–55], purely initial state descriptions have thus far struggled to fully reproduce quantitative and qualitative features of the data [38,39]. Some have, potentially prematurely, “ruled out” initial-stage Glasma correlations [56]; however, they should be present and can in principle affect observables, even when geometry driven final state effects dominate.

In the IP-Glasma + MUSIC + UrQMD model [55], initial state anisotropies from both the Glasma and the final state response to the geometry are present. Their relative contributions were analyzed as functions of multiplicity in [10], and an observable that should be able to distinguish them as sources of the observed anisotropies—namely, the correlation of the elliptic anisotropy with the mean transverse momentum—was analyzed in [57]. The results in these works indicate that, while the initial state anisotropy has a non-negligible contribution over a wide range of multiplicities, it starts to be the dominant contribution only for $dN_{\text{ch}}/d\eta \lesssim 5$ –10, approximately independent of the collision system or energy.

*prasingh@jyu.fi

Thus far, many calculations for proton-nucleus collisions, including the aforementioned ones, have been performed under the assumption of boost invariance, which means that correlations of both the transverse geometry and the initial momentum anisotropy extend over arbitrarily large separations in rapidity. In this work we relax the assumption of boost invariance and set out to explore the longitudinal dependence of both the initial state geometry and initial state momentum space correlations. This will provide important input to experimentally distinguish the two types of signals from each other and from short-range “nonflow” contributions that result, e.g., from minijets or resonance decays.

This paper is organized as follows. We start with a brief description of the 3D IP-Glasma model in Sec. II and subsequently discuss some global event properties in 5.02 TeV p + Pb collisions in Sec. III. Our main results regarding the longitudinal dependence of the initial state geometry and initial state momentum space correlations are presented in Sec. IV. We conclude and present an outlook in Sec. V.

II. THE 3D IP-GLASMA MODEL

We follow the description of [58], which is built on the high-energy factorization of the expectation values of sufficiently inclusive quantities [59,60]. Based on the color glass condensate effective field theory of high-energy QCD [61], observables $O(y_{\text{obs}})$ at a rapidity y_{obs} can be calculated on an event-by-event basis

$$O(y_{\text{obs}}) = O_{\text{cl}}(V_{\mathbf{x}_\perp}^{\text{p}}(+y_{\text{obs}}), V_{\mathbf{x}_\perp}^{\text{Pb}}(-y_{\text{obs}})), \quad (1)$$

as a functional of the lightlike Wilson lines $V_{\mathbf{x}_\perp}^{\text{p}}(+y_{\text{obs}})$ and $V_{\mathbf{x}_\perp}^{\text{Pb}}(-y_{\text{obs}})$ of the projectile (p) and target (Pb), by solving the classical Yang-Mills (CYM) equations. Starting from the initial conditions $V_{\mathbf{x}_\perp}^{\text{p/Pb}}(-Y_{\text{max}})$ determined by the IP-Glasma model [62,63] at the maximal observed rapidity Y_{max} , the rapidity evolution of the lightlike Wilson lines $V_{\mathbf{x}_\perp}^{\text{p/Pb}}(Y)$ is calculated using the Jalilian-Marian-Iancu-McLerran-Weigert-Leonidov-Kovner (JIMWLK) evolution equation [64–68]. Based on Eq. (1), the observables at each rapidity are computed from the solutions to the classical field equations, while the longitudinal (rapidity) structure is governed by the small- x evolution of the Wilson lines. While such factorization, as in Eq. (1), has been proven only for inclusive quantities which encompass measurements at a single rapidity [59,60], we will use the same prescription to calculate unequal rapidity correlations on an event-by-event basis. We refer to [58] for additional discussions of the associated caveats and provide details of the implementation of the 3D-Glasma model below.

A. IP-Glasma initial condition

Within the color glass condensate the small- x gluon fields of the incoming nuclei are generated by the moving valence charges according to the Yang-Mills equations

$$[D_\mu, F^{\mu\nu}] = J^\nu, \quad (2)$$

where $D_\mu = \partial_\mu - igA_\mu$ is the gauge covariant derivative and $F^{\mu\nu} = \frac{i}{g}[D^\mu, D^\nu] = \partial^\mu A^\nu - \partial^\nu A^\mu - ig[A^\mu, A^\nu]$ is the field strength tensor, with the gluon fields $A^\mu = A_a^\mu t^a$. The t^a are the generators of $SU(N_c)$ (for the number of colors $N_c = 3$) in the fundamental representation. The index a is the color index and runs from 1 to $(N_c^2 - 1) = 8$. The eikonal currents J^ν on the right-hand side of Eq. (2) are given by the sum of the color currents of the two nuclei (the moving large- x degrees of freedom),

$$J^\nu = \delta^{\nu+} \rho_{\text{Pb}}(\mathbf{x}_\perp) \delta(x^-) + \delta^{\nu-} \rho_{\text{p}}(\mathbf{x}_\perp) \delta(x^+). \quad (3)$$

We will use the IP-Glasma model to determine the color charge densities $\rho_{\text{p/Pb}}(\mathbf{x}_\perp)$ and associated Wilson lines at the initial rapidities (the largest x values). Wilson lines at smaller x then follow from JIMWLK evolution, as discussed in the next subsection.

In IP-Glasma the color charges $\rho_{\text{Pb}}(\mathbf{x}_\perp)$ and $\rho_{\text{p}}(\mathbf{x}_\perp)$ are sampled on an event-by-event basis, assuming local Gaussian correlations as in the McLerran-Venugopalan (MV) model [69,70]. In practice, one determines the Wilson lines $V_{\mathbf{x}_\perp}$ for each nucleus numerically, approximating the path ordered exponential with the product [71],

$$V_{\mathbf{x}_\perp}^{\text{Pb/p}} = \prod_{k=1}^{N_y} \exp\left(-ig \frac{\rho_{\text{Pb/p}}^k(\mathbf{x}_\perp)}{\nabla^2 - \tilde{m}^2}\right), \quad (4)$$

where $\tilde{m} = 0.2$ GeV (or 0.8 GeV as indicated) is an infrared regulator that is used to avoid unphysical Coulomb tails, $N_y = 50$ is the number of slices in the longitudinal direction, and, as in the MV model, ρ_{Pb}^k and ρ_{p}^k have zero mean and their two-point functions satisfy (suppressing the subscripts Pb and p for clarity)

$$\langle \rho_i^a(\mathbf{b}_\perp) \rho_j^b(\mathbf{x}_\perp) \rangle = \frac{g^2 \mu^2(x, \mathbf{b}_\perp)}{N_y} \delta^{ab} \delta^{ij} \delta^{(2)}(\mathbf{b}_\perp - \mathbf{x}_\perp). \quad (5)$$

Spatially (\mathbf{b}_\perp) dependent color charge densities, $g^2 \mu_{\text{Pb/p}}^2(x, \mathbf{b}_\perp) = c_{Q_s} Q_s^{\text{Pb/p}}(x, T(\mathbf{b}_\perp))^1$, are determined using the IPSat model [72,73], which provides the saturation scale $Q_s(x, T(\mathbf{b}_\perp))$ as a function of the nuclear thickness $T(\mathbf{b}_\perp)$ at a given Bjorken x . The nuclear thickness functions $T(\mathbf{b}_\perp)$, which provide the \mathbf{b}_\perp dependence,

¹We employ $c_{Q_s} = 1.25$ for $\tilde{m} = 0.2$ GeV and $c_{Q_s} = 1.82$ for $\tilde{m} = 0.8$ GeV.

are determined as in [55] by sampling the position of individual nucleons from a Woods-Saxon distribution in the case of the Pb nucleus. Subsequently, the position of $N_q = 3$ hot spots per nucleon is assigned according to a two-dimensional Gaussian distribution with width B_p , and each hot spot is assigned a two-dimensional Gaussian thickness profile of width B_q . The parameters $B_p = 4 \text{ GeV}^{-2}$ and $B_q = 0.3 \text{ GeV}^{-2}$ of the model are constrained using deeply inelastic scattering data on protons from HERA [74]. Once the nuclear thickness $T(\mathbf{b}_\perp)$ is determined, we self-consistently determine $Q_s(x, \mathbf{b}_\perp)$ by iteratively solving for

$$x = x(\mathbf{b}_\perp) = \frac{Q_s(x, T(\mathbf{b}_\perp))}{\sqrt{s_{\text{NN}}}} e^{-Y}, \quad (6)$$

where $\sqrt{s_{\text{NN}}}$ is the center of mass energy of the collision. We note that the public IP-Glasma code employed in this study can be found at [75], and we refer the reader to [55] for a detailed description of the implementation used in this work.

Based on the above procedure, we generate a total of $N_p = 32$ and $N_{\text{Pb}} = 8$ configurations of the Wilson lines $V_{\mathbf{x}_\perp}^{\text{p/Pb}}(-Y_{\text{max}})$ of the protons and lead nuclei at the largest x value, corresponding to the initial rapidity $Y = -Y_{\text{max}} = -2.4$, with transverse coordinates (\mathbf{x}_\perp) discretized on an $N_s \times N_s$ lattice with $N_s = 1024$ sites and lattice spacing $a_s = 0.02 \text{ fm}$.

B. JIMWLK evolution

Starting from the IP-Glasma initial conditions for the Wilson lines $V_{\mathbf{x}_\perp}^{\text{p/Pb}}(-Y_{\text{max}})$, we perform the JIMWLK [64–68] evolution from $Y = -2.4$ to $Y = +2.4$ for each configuration of the proton and the lead nucleus. We store the configurations for various slices in rapidity in steps of $Y = 0.2$.

The implementation of the JIMWLK solver is equal to that discussed in [58]. Specifically, we express the JIMWLK hierarchy in terms of a functional Langevin equation for the Wilson lines [76,77]. Each Langevin step can be written as [78]

$$V_{\mathbf{x}_\perp}(Y + dY) = \exp\left\{-i \frac{\sqrt{\alpha_s dY}}{\pi} \int_{\mathbf{z}_\perp} K_{\mathbf{x}_\perp - \mathbf{z}_\perp} \cdot (V_{\mathbf{z}_\perp} \boldsymbol{\xi}_{\mathbf{z}_\perp} V_{\mathbf{z}_\perp}^\dagger)\right\} \times V_{\mathbf{x}_\perp}(Y) \exp\left\{i \frac{\sqrt{\alpha_s dY}}{\pi} \int_{\mathbf{z}_\perp} K_{\mathbf{x}_\perp - \mathbf{z}_\perp} \cdot \boldsymbol{\xi}_{\mathbf{z}_\perp}\right\}, \quad (7)$$

with Gaussian white noise $\boldsymbol{\xi}_{\mathbf{z}_\perp} = (\xi_{\mathbf{z}_\perp,1}^a t^a, \xi_{\mathbf{z}_\perp,2}^a t^a)$ that is local in transverse coordinate, color, and rapidity, i.e., $\langle \xi_{\mathbf{z}_\perp,i}^b(Y) \rangle = 0$ and

$$\langle \xi_{\mathbf{x}_\perp,i}^a(Y) \xi_{\mathbf{y}_\perp,j}^b(Y') \rangle = \delta^{ab} \delta^{ij} \delta_{\mathbf{x}_\perp \mathbf{y}_\perp}^{(2)} \delta(Y - Y'). \quad (8)$$

Since we are particularly interested in the impact parameter dependence, we follow [79] and employ a regularized JIMWLK kernel

$$K_{\mathbf{x}_\perp - \mathbf{z}_\perp} = m |\mathbf{x}_\perp - \mathbf{z}_\perp| K_1(m |\mathbf{x}_\perp - \mathbf{z}_\perp|) \frac{\mathbf{x}_\perp - \mathbf{z}_\perp}{(\mathbf{x}_\perp - \mathbf{z}_\perp)^2}, \quad (9)$$

which suppresses emission at large distance scales and limits growth in impact parameter space. The modified Bessel function of the second kind $K_1(x)$ behaves as $x K_1(x) = 1 + \mathcal{O}(x^2)$ for small arguments x , leaving the kernel unmodified at short distance scales. Conversely, for large arguments $K_1(x) = \sqrt{\frac{\pi}{2x}} e^{-x}$ decays exponentially, suppressing gluon emissions at large distance scales. This regularization also prevents the unphysical exponential growth of the cross section, which would violate unitarity [80].

We note that the only free parameters controlling the JIMWLK evolution in Eq. (7) are the (fixed) coupling constant α_s and the infrared regulator m , and we will consider variations of both parameters to assess the sensitivity of our results. We illustrate the JIMWLK evolution of the spatial configuration of three sample protons in Fig. 1, where we plot the trace of the Wilson lines, $1 - \text{Re}[\text{tr}(V_{\mathbf{x}_\perp})]/N_c$, for five different rapidities. Going left to right, x decreases for the left moving proton. One can see that the average size of the proton grows with the evolution and that shorter scale structures emerge as Q_s grows with decreasing x . This is expected, as the correlation length in the transverse plane behaves as $\sim 1/Q_s$. Similar features can be observed for the evolution of the lead nuclei, shown in Fig. 2, where for the right moving nucleus x decreases going from right to left; in addition, the impact parameters of the protons, for events within a given centrality class (see Sec. II D), are marked with different colored circles.

C. Event generation and classical Yang-Mills evolution

Having determined N_p proton configurations and N_{Pb} lead configurations over the entire range of rapidities $-2.4 \leq Y \leq 2.4$, we proceed to generate events where, for each of the $N_p \times N_{\text{Pb}}$ combinations of protons and lead nuclei, we perform $N_{\text{b}_\perp} = 16$ collisions with different impact parameters \mathbf{b}_\perp , sampled according to a two-dimensional uniform distribution with the restriction $0 < |\mathbf{b}_\perp| < 8 \text{ fm}^2$. Based on the JIMWLK evolved Wilson lines, the initial conditions for the nonvanishing components of the gauge fields $A_{\mathbf{x}_\perp}^i(\tau = 0^+)$, $E_{\mathbf{x}_\perp}^a(\tau = 0^+)$ in the forward light cone at a given rapidity y_{obs} are then given by

²Note that in order to avoid interpolation of the $SU(N_c)$ matrices, we round the impact parameter \mathbf{b}_\perp to the next lattice site.

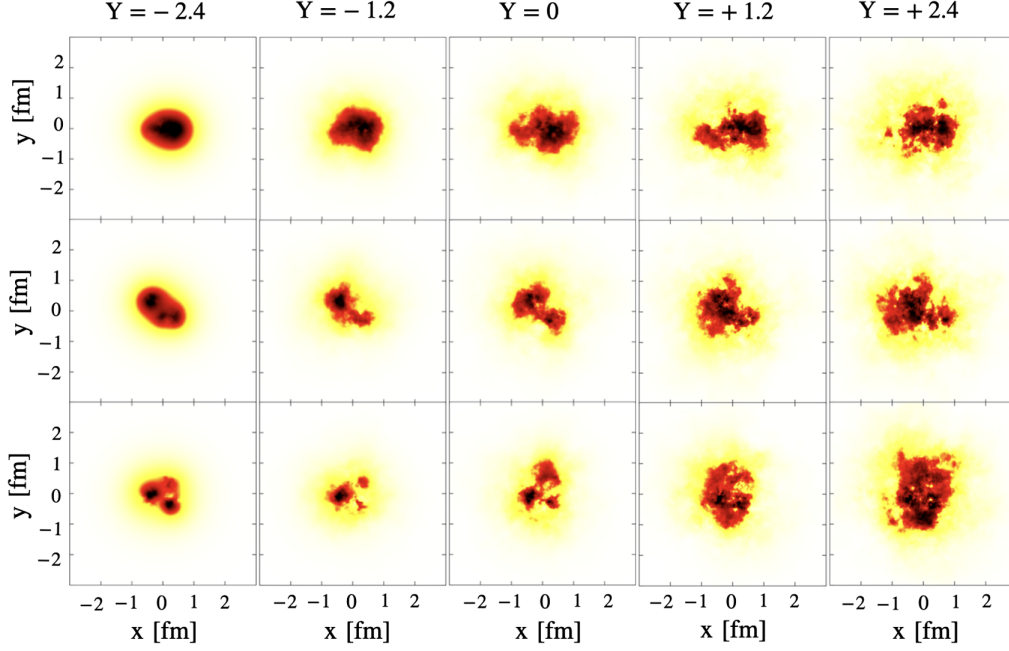


FIG. 1. JIMWLK evolution of the gluon fields in three different configurations of the proton for $m = 0.2$ GeV and $\alpha_s = 0.3$. The trace of Wilson lines $1 - \text{Re}[\text{tr}(V_{x_\perp})]/N_c$ is shown in the transverse plane for different rapidities (Y) to illustrate the emergence of finer structure and growth of the proton with increasing rapidity.

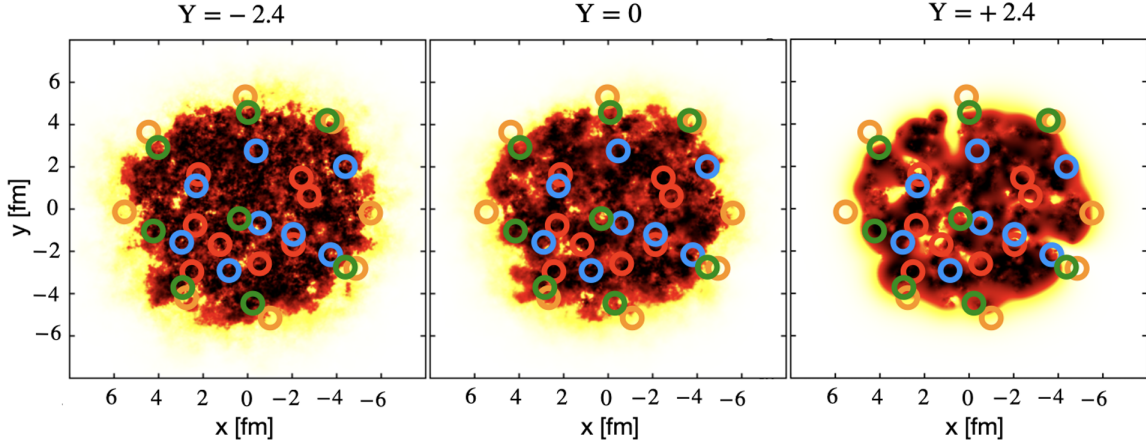


FIG. 2. View of the transverse plane for a particular configuration of a right moving lead nucleus at three different rapidities. Circles indicate the collision point of the proton with this lead nucleus for a selection of events. The color coding indicates the centrality class of the event: red (0–5)%, blue (40–50)%, green (60–70)%, and orange (80–90)% (for the definition of centrality, see Sec. IID).

$$A_{\mathbf{x}_\perp}^i(\tau = 0^+, y_{\text{obs}}) = \frac{i}{g} [(V_{\mathbf{x}_\perp}^{\text{p}}(+y_{\text{obs}}) \partial^i V_{\mathbf{x}_\perp}^{\text{p}\dagger}(+y_{\text{obs}})) + (V_{\mathbf{x}_\perp + \mathbf{b}_\perp}^{\text{Pb}}(-y_{\text{obs}}) \partial^i V_{\mathbf{x}_\perp + \mathbf{b}_\perp}^{\text{Pb}\dagger}(-y_{\text{obs}}))], \quad (10)$$

$$E_{\mathbf{x}_\perp}^\eta(\tau = 0^+, y_{\text{obs}}) = \frac{i}{g} [(V_{\mathbf{x}_\perp}^{\text{p}}(+y_{\text{obs}}) \partial^i V_{\mathbf{x}_\perp}^{\text{p}\dagger}(+y_{\text{obs}})), (V_{\mathbf{x}_\perp + \mathbf{b}_\perp}^{\text{Pb}}(-y_{\text{obs}}) \partial^i V_{\mathbf{x}_\perp + \mathbf{b}_\perp}^{\text{Pb}\dagger}(-y_{\text{obs}}))]. \quad (11)$$

Starting from the lattice discretized version of the initial conditions in Eqs. (10) and (11) [81], we solve the lattice discretized CYM equations of motion up to time $\tau = 0.2$ fm/c, at which we determine the energy-momentum tensor $T^{\mu\nu}$ (see, e.g., [55] for how we compute $T^{\mu\nu}$ on the lattice), gluon spectra $\frac{dN_g}{d^2\mathbf{p}_\perp dy}$, and gluon multiplicity $dN_g/dy = \int d^2\mathbf{p}_\perp \frac{dN_g}{d^2\mathbf{p}_\perp dy}$. The gluon spectra at a particular time τ are obtained by projecting the gauge fixed equal time correlation functions onto transversely polarized gluon modes, as described in [33]:

$$\frac{dN}{d^2\mathbf{p}_\perp dy} = \frac{1}{(2\pi)^2} \sum_{\lambda,a} |\tau g^{\mu\nu}(\xi_\mu^{\lambda,\mathbf{p}_\perp}(\tau) \partial_\tau A_\nu^a(\tau, \mathbf{p}_\perp))|^2, \quad (12)$$

where $g^{\mu\nu}(1, -1, -1, -\tau^{-2})$ denotes the Bjorken metric and $\lambda = 1, 2$ labels the two transverse polarizations. The mode function takes the following form in the Coulomb gauge:

$$\xi_\mu^{1,\mathbf{p}_\perp}(\tau) = \frac{\sqrt{\pi}}{2|\mathbf{p}_\perp|} \begin{pmatrix} -p_y \\ p_x \\ 0 \end{pmatrix} H_0^{(2)}(|\mathbf{p}_\perp|\tau), \quad (13)$$

$$\xi_\mu^{2,\mathbf{p}_\perp}(\tau) = \frac{\sqrt{\pi}}{2|\mathbf{p}_\perp|} \begin{pmatrix} 0 \\ 0 \\ \mathbf{p}_\perp \cdot \boldsymbol{\tau} \end{pmatrix} H_1^{(2)}(|\mathbf{p}_\perp|\tau), \quad (14)$$

where $H_p^{(2)}$ are the Hankel functions of the second kind and order p .

Based on the factorization formula in Eq. (1), the rapidity y_{obs} dependence of these observables in each event is then calculated as in [58] from a series of independent 2 + 1D CYM simulations, which according to Eqs. (10) and (11) start from the same Wilson lines $V_{\mathbf{x}_\perp}^{\text{p}}$ and $V_{\mathbf{x}_\perp}^{\text{Pb}}$ evolved up to different rapidities $Y = \pm y_{\text{obs}}$. We will consider a rapidity range $y_{\text{obs}} \in [-2.4, +2.4]$, where $y_{\text{obs}} = -2.4(+2.4)$ corresponds to no JIMWLK evolution in the proton (lead nucleus), and calculate observables in intervals of $\Delta y = 0.4$.

D. Gluon multiplicity and centrality selection

Based on the above procedure, we obtain a total of $N_{\text{events}} = N_{\text{b}_\perp} \times N_{\text{p}} \times N_{\text{Pb}} = 4096$ events, which we further classify into centrality classes according to their gluon multiplicity $g^2 dN_g/dy|_{y_{\text{obs}}=0}$ at midrapidity $y_{\text{obs}} = 0$. Since we do not invoke any collision criteria (e.g., $N_{\text{coll}} \geq 1$), we first disregard events with $g^2 dN_g/dy|_{y_{\text{obs}}=0} < 4$ from our event selection and subsequently perform the usual binning.

We present the gluon multiplicity distribution at midrapidity ($y = 0$) in Fig. 3, where we have scaled the distribution by the mean multiplicity in order to compare it to experimental data on the uncorrected reconstructed primary tracks from the CMS Collaboration [82]. Different curves in Fig. 3 show the results for two different sets of parameters, namely, $m = \tilde{m} = 0.2$ GeV with $c_{Q_s} = 1.25$ and $m = \tilde{m} = 0.8$ GeV with $c_{Q_s} = 1.82$, which we will continue to investigate in the following. While in both cases the width of the gluon multiplicity distribution agrees well with that of the experimental data on reconstructed tracks, we find that for $m = \tilde{m} = 0.2$ GeV the computed gluon distribution has some peak and dip structures at small multiplicities, which can be attributed to very peripheral events and is not seen in the experimental data. Nevertheless, even in this case, for larger multiplicities

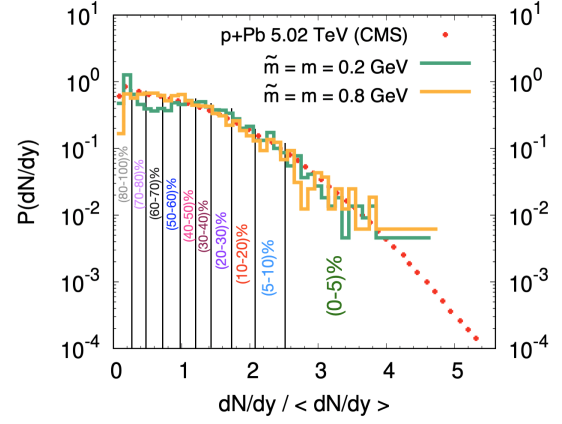


FIG. 3. Histogram for the gluon multiplicity distribution $g^2 dN_g/dy$ normalized by its expectation value $\langle g^2 dN_g/dy \rangle$ at midrapidity ($y = 0$). Simulations are done for two different sets of parameters, $m = \tilde{m} = 0.2$ GeV with $c_{Q_s} = 1.25$ and $m = \tilde{m} = 0.8$ GeV with $c_{Q_s} = 1.82$, along with $\alpha_s = 0.15$. Crosses represent experimental charged hadron distribution data dN_{ch}/dy for raw reconstructed primary tracks in $\sqrt{s} = 5.02$ TeV p + Pb collisions from the CMS Collaboration [82]. Centrality classes are indicated by the vertical lines.

(equal or greater than the mean) the data are well described. Figure 3 also indicates the centrality classes as obtained from the gluon distribution.

III. GLOBAL EVENT STRUCTURE AND NATURE OF HIGH-MULTIPLICITY EVENTS

Before we discuss the event-by-event geometry and azimuthal correlations, it will be insightful to briefly comment on the general features of low- and high-multiplicity events in high-energy p + Pb collisions. We first study the rapidity dependence of the multiplicity dN_g/dy and transverse energy dE_\perp/dy .³ The various panels in Fig. 4 show the rapidity dependence of dN_g/dy and dE_\perp/dy normalized to their value at midrapidity $dN_g/dy|_{y=0}$ for different centrality classes (0–5)%, (40–50)%, (60–70)%, and (80–90)% for the two different sets of parameters $m = \tilde{m} = 0.2$ GeV with $c_{Q_s} = 1.25$ and $m = \tilde{m} = 0.8$ GeV with $c_{Q_s} = 1.82$. Absolute values of the multiplicities and transverse energy per unit rapidity at midrapidity are provided in Table I.

Generally, one can see that the rapidity dependence of both the multiplicity dN_g/dy and the transverse energy dE_\perp/dy flattens as one approaches more peripheral events; however, a comparison of the left and right panels indicates that the magnitude of the forward-backward asymmetry in more central events is actually quite sensitive to the value of

³We assume that space-time rapidity is equal to the momentum rapidity, $\eta_s = y$, which holds for a system, where the phase-space density of gluons is proportional to $\delta(\eta_s - y)$ [15]. For this reason, we will be using η_s and y interchangeably.

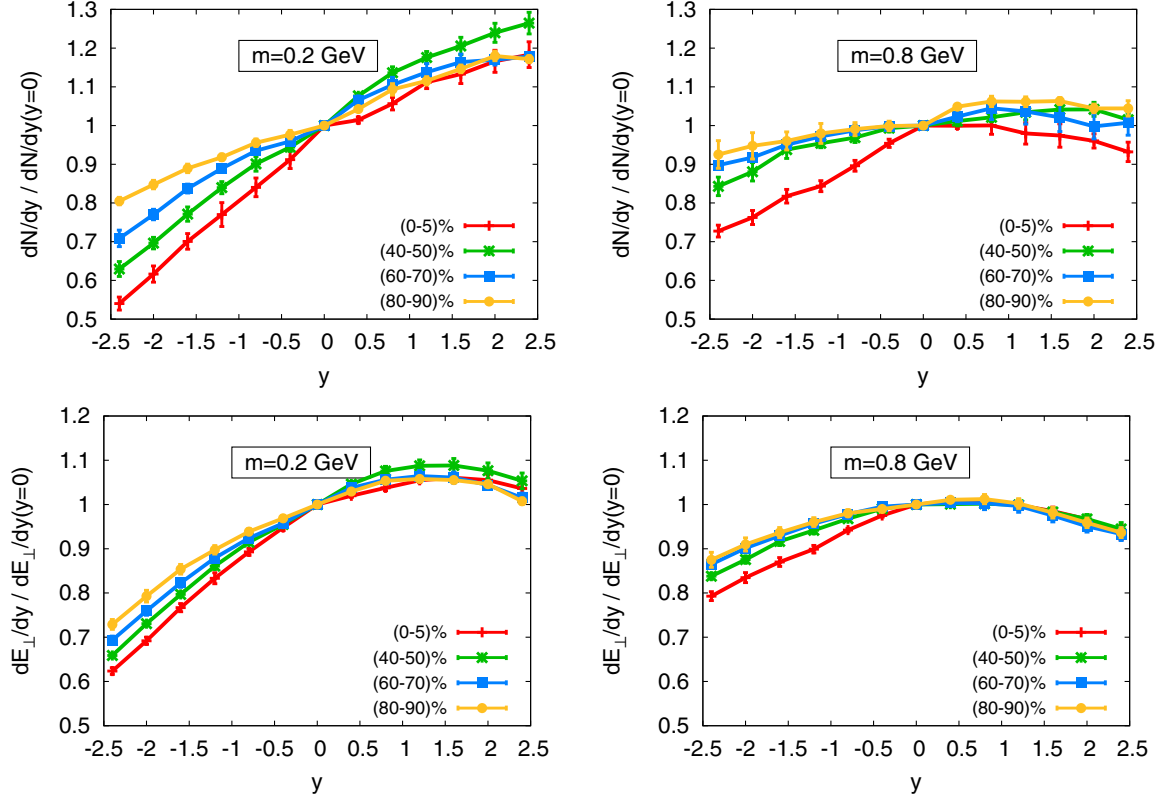


FIG. 4. Gluon multiplicity dN_g/dy (top panels) and transverse energy per unit rapidity $dE_\perp/dy \propto \tau \epsilon(\tau = 0.2 \text{ fm})$ (bottom panels) relative to their values at midrapidity for different centrality classes. The simulation parameters are $\alpha_s = 0.15$, $\tilde{m} = m = 0.2 \text{ GeV}$ (left panels), and $\tilde{m} = m = 0.8 \text{ GeV}$ (right panels).

the infrared regulators m and \tilde{m} . Evidently, it would be instructive to compare the results in Fig. 4 to experimental measurements; however, we are not aware of measurements of dN/dy of identified hadrons in p + Pb collisions. Nevertheless, when comparing our results for the gluon rapidity distribution to $dN_{\text{ch}}/d\eta$ of unidentified charged hadrons, we find that the gluon distribution for $m = \tilde{m} = 0.2 \text{ GeV}$ generally shows a steeper rapidity dependence than the experimental data from the ALICE Collaboration [83], which is essentially symmetric in the (80–100)% bin

TABLE I. Values for gluon multiplicity $g^2 dN/dy$ and transverse energy per unit rapidity $g^2 dE_\perp/dy$ at $y = 0$ for $\alpha_s = 0.15$ together with the ALICE data [83] for $dN_{\text{ch}}/d\eta$. Simulation results are obtained for two different setups, $\tilde{m} = m = 0.2 \text{ GeV}$ with $c_{Q_s} = 1.25$, and $\tilde{m} = m = 0.8 \text{ GeV}$ with $c_{Q_s} = 1.82$.

$g^2 dN_g/dy$	0%–5%	40%–50%	60%–70%	80%–90%
$m = 0.2 \text{ GeV}$	141.1	52.9	29.2	9.2
$m = 0.8 \text{ GeV}$	152.3	51.2	33.2	16.6
ALICE $dN_{\text{ch}}/d\eta$	42.6	16.1	9.6	4.3
$g^2 dE_\perp/dy \text{ (GeV)}$				
$m = 0.2 \text{ GeV}$	457.1	162.6	80.1	20.1
$m = 0.8 \text{ GeV}$	697.1	214.4	136.7	66.2

and appears to be more in line with the behavior observed for $m = \tilde{m} = 0.8 \text{ GeV}$.

By comparing the left and right panels of Fig. 4, one finds a 20%–30% difference when varying the infrared regulators m and \tilde{m} by a factor of 4, which provides an estimate of the systematic uncertainty of the calculation.

While the self-normalized quantities in Fig. 4 emphasize the rapidity dependence, we note that, for both parameter sets, the centrality dependence of the absolute yield at midrapidity up to 60%–70% is approximately in line with that of the experimentally determined charged hadron yield, as can be seen in Table I.

When comparing the top and bottom panels of Fig. 4, one observes that the transverse energy shows a slightly weaker centrality dependence relative to the gluon multiplicity. This is likely a consequence of the transverse energy being more sensitive to the larger of the two saturation scales Q_s , as parametrically one has $dN_g/dy \sim Q_s^2 < S_\perp$, while $dE_\perp/dy \sim Q_{s>} Q_s^2 < S_\perp$ [84,85], where S_\perp is the transverse area and $Q_{s>}/<$ denotes the larger/smaller of the two saturation scales.

Next, in order to obtain further insight into the properties of low- and high-multiplicity events, we will extract the average Pb and p saturation scales $Q_s(y)$ and determine a measure of the system size $S_\perp(y)$ for the different centrality

classes. Specifically, the saturation scale $Q_s(y)$ is extracted from the dipole scattering amplitude

$$D(\mathbf{r}_\perp, \mathbf{d}_\perp) = \frac{1}{N_c} \text{tr} [V_{\mathbf{d}_\perp + \mathbf{r}_\perp/2} V_{\mathbf{d}_\perp - \mathbf{r}_\perp/2}^\dagger], \quad (15)$$

averaged over (dipole) impact parameters $|\mathbf{d}_\perp| < 0.2R_p$ from the collision point⁴ (see the Appendix for details). By following previous works [79], we extract the distance $|\mathbf{r}_\perp|_c$, where the dipole amplitude exceeds a value of c , i.e.,

$$D(|\mathbf{r}_\perp|_c, |\mathbf{d}_\perp| < 0.2R_p) = c, \quad (16)$$

and calculate $Q_s = 2/|\mathbf{r}_\perp|_c \log^{1/2}(1/c)$ according to the parametrization $D(\mathbf{r}_\perp) = \exp(-Q_s^2 \mathbf{r}_\perp^2/4)$. We employ $c = 0.8$ and 0.9 to estimate the uncertainty of this procedure. While the saturation scale Q_s is a property of the projectile and target, the centrality dependence stems simply from the fact that larger values of $Q_s^{p/Pb}$ give rise to a larger multiplicity, corresponding to lower centrality, and we determine $Q_s^{p/Pb}$ separately for each centrality class.

The system size S_\perp is determined from the energy-momentum tensor $T^{\mu\nu}$ as

$$S_\perp = \frac{\int d^2\mathbf{x}_\perp \mathbf{x}_\perp^2 T^{\tau\tau}(\mathbf{x}_\perp)}{\int d^2\mathbf{x}_\perp T^{\tau\tau}(\mathbf{x}_\perp)}, \quad (17)$$

which we evaluate at $\tau = 0.2$ fm/c after the collision of the proton and the lead nucleus.

We will focus on the case $m = \tilde{m} = 0.2$ GeV, which exhibits a stronger rapidity and centrality dependence of dN/dy and dE_\perp/dy . For this case our results for $Q_s^{p/Pb}(y)$ and $S_\perp(y)$ are compactly summarized in Fig. 5. With decreasing x , which corresponds to an increasing rapidity y for the left moving proton and a decreasing rapidity y for the right moving lead nucleus, both saturation scales Q_s increase due to the JIMWLK evolution. The proton saturation scale Q_s^p is similar in the three more peripheral events, while the nucleus' Q_s^{Pb} depends more strongly on centrality, indicating that in mid-central and peripheral events the multiplicity is determined by the impact parameter, i.e., the position in the lead nucleus where the proton hits, as well as fluctuations in the lead nucleus. In contrast, the proton saturation scale in the most central bin is significantly larger than for the other centralities, while there is little difference between the lead saturation scale in the 40%–50% and 0%–5% centrality classes. This means

⁴By the collision point we mean the transverse position where the center of mass of the proton hits the lead nucleus. Hence, for the proton the dipole amplitude is extracted around its center of mass, while, according to Eqs. (10) and (11) for the lead nucleus, the collision point is offset from the center of the nucleus and the dipole amplitude is thus measured around the impact parameter \mathbf{b}_\perp of the p + Pb collision.

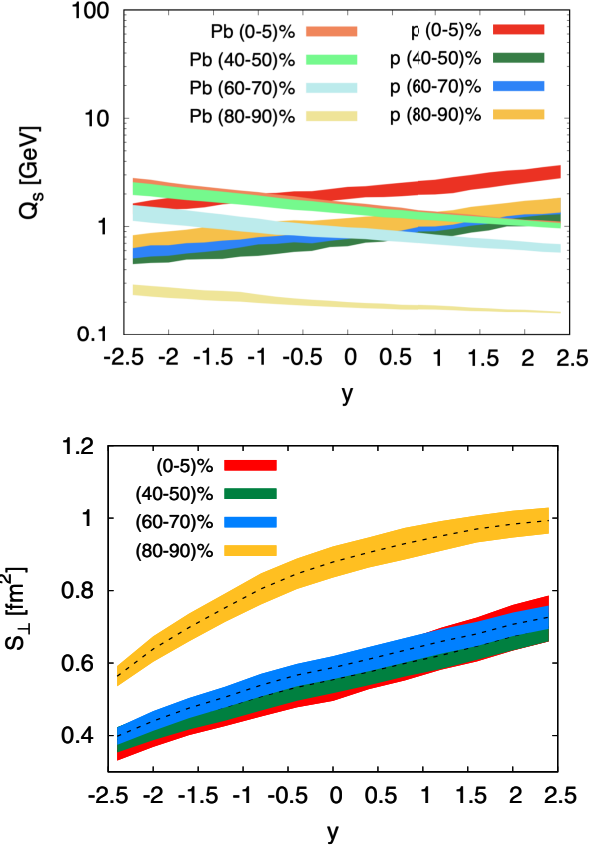


FIG. 5. Top panel: saturation scale $Q_s(y)$ as a function of rapidity y for proton (p) and lead (Pb) nucleus for different centrality classes. Bottom panel: rapidity dependence of the system size S_\perp for various centrality classes. Results are for $a_s = 0.15$ and $m = 0.2$ GeV.

that the highest multiplicities are reached by upward fluctuations of the proton's gluon density quantified by Q_s^p .

The size of the interaction region increases approximately linearly (for the three most central centralities studied), which is driven by the growth of the proton size with rapidity [79,80] (see the Appendix). The most peripheral events show a significantly larger area, which may appear counterintuitive at first sight. However, given the definition of the area measure in Eq. (17), an overall very small but spread out energy density can lead to a large area, which seems to be the dominant structure of the most peripheral events that we studied. For all other centralities, the area is approximately the same, and the difference in multiplicity is driven almost entirely by changes in the Q_s values.

IV. EVENT GEOMETRY AND INITIAL STATE MOMENTUM CORRELATIONS

Having established the basic features of the events in different centrality classes, we continue by investigating the longitudinal structure of the event geometry and the initial state momentum anisotropy. We follow standard procedure

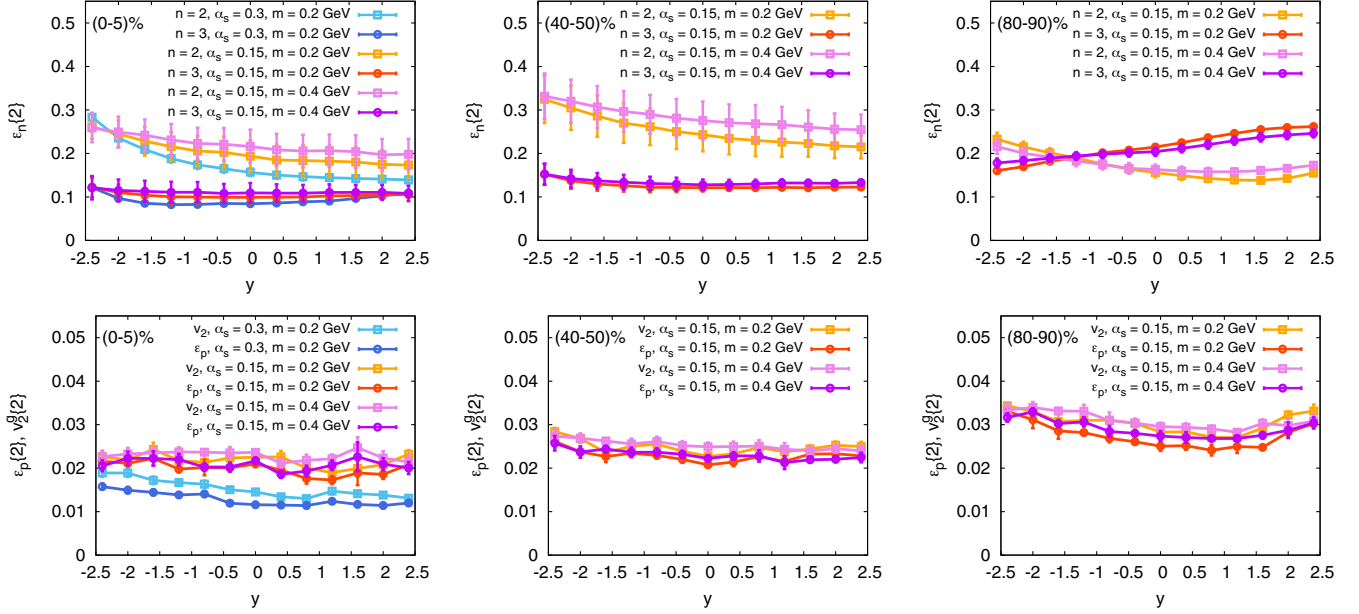


FIG. 6. Geometric eccentricities $\varepsilon_n\{2\} = \sqrt{\langle |\varepsilon_n(y)|^2 \rangle}$ (top row) and initial momentum anisotropies $\varepsilon_p\{2\} = \sqrt{\langle |\varepsilon_p(y)|^2 \rangle}$ together with azimuthal anisotropy $v_2^g\{2\} = \sqrt{\langle |v_2^g(y)|^2 \rangle}$ (bottom row) for different centrality classes 0%–5% (left panels), 40%–50% (center panels), and 80%–90% (right panels) as a function of rapidity.

and characterize the event geometry in terms of the eccentricities

$$\varepsilon_n(y) = \frac{\int d^2\mathbf{r}_\perp T^{\tau\tau}(y, \mathbf{r}_\perp) |\mathbf{r}_\perp|^n e^{in\phi_{\mathbf{r}_\perp}}}{\int d^2\mathbf{r}_\perp T^{\tau\tau}(y, \mathbf{r}_\perp) |\mathbf{r}_\perp|^n}, \quad (18)$$

where the integer n indicates the harmonic. We will study the cases $n = 2$ and $n = 3$.

Similarly, following [10,57], the initial state momentum anisotropy can be characterized in terms of the anisotropic energy flow

$$\varepsilon_p(y) = \frac{\int d^2\mathbf{r}_\perp T^{xx}(y, \mathbf{r}_\perp) - T^{yy}(y, \mathbf{r}_\perp) + 2iT^{xy}(y, \mathbf{r}_\perp)}{\int d^2\mathbf{r}_\perp T^{xx}(y, \mathbf{r}_\perp) + T^{yy}(y, \mathbf{r}_\perp)} \quad (19)$$

or, alternatively, as in [33] in terms of the azimuthal anisotropy v_2^g of the produced gluons⁵

$$v_2^g(y) = \frac{\int d^2\mathbf{k}_\perp |\mathbf{k}_\perp| \frac{dN_g}{dy d^2\mathbf{k}_\perp}(y) e^{2i\phi_{\mathbf{k}_\perp}}}{\int d^2\mathbf{k}_\perp |\mathbf{k}_\perp| \frac{dN}{dy d^2\mathbf{k}_\perp}(y)}. \quad (20)$$

We evaluate the expressions in Eqs. (18)–(20) at $\tau = 0.2$ fm/c to calculate ε_n , ε_p , and v_2^g as functions of rapidity y on an event-by-event basis. Subsequently, to quantify the

⁵We note that the additional $|\mathbf{k}_\perp|$ weight is chosen such that in the quasiparticle picture the definitions of ε_p and v_2^g agree with each other.

overall rapidity dependence we compute the correlation functions

$$C_{\mathcal{O}}(y_1, y_2) = \langle \text{Re}(\mathcal{O}(y_1) \mathcal{O}^*(y_2)) \rangle, \quad (21)$$

where $\langle \cdot \rangle$ denotes an event average and \mathcal{O} is any of the above observables. The correlation function $C_{\mathcal{O}}$ contains information about both the magnitude and the rapidity dependence of the correlation function. To focus on the rapidity decorrelation of the transverse geometry and initial state momentum correlations, we will also show results for the normalized rapidity correlation function

$$C_{\mathcal{O}}^N(y_1, y_2) = \frac{C_{\mathcal{O}}(y_1, y_2)}{\sqrt{\langle |\mathcal{O}(y_1)|^2 \rangle \langle |\mathcal{O}(y_2)|^2 \rangle}}. \quad (22)$$

A. Rapidity dependence of event geometry and momentum anisotropy

In Fig. 6 (top row) we show the rapidity dependence of eccentricities $\varepsilon_2\{2\}(y) = \sqrt{\langle |\varepsilon_2(y)|^2 \rangle}$ and $\varepsilon_3\{2\}(y) = \sqrt{\langle |\varepsilon_3(y)|^2 \rangle}$ for different parameters and centrality classes. In most cases ε_2 decreases with increasing rapidity, and does so more rapidly for larger α_s and smaller m , as expected because of how these parameters affect the JIMWLK evolution speed. For our standard parameters of $\tilde{m} = m = 0.2$ GeV and $\alpha_s = 0.15$, the rapidity dependence is rather weak. For the most peripheral bin, ε_2 has a shallow minimum as a function of rapidity. The triangularity ε_3 has an even weaker rapidity dependence than ε_2 in

the two more central bins and increases with increasing rapidity in the most peripheral bin. Given the comparable size of ε_2 and ε_3 in this bin, one might expect the observed anticorrelation between the two quantities, as it is difficult geometrically to generate a large ε_2 and ε_3 at the same time. (This can be seen most easily when one arranges just three hot spots. A maximal triangularity goes along with a reduced ellipticity, and vice versa.)

The bottom panel in Fig. 6 shows the rapidity dependence of the initial state anisotropy $\varepsilon_p\{2\}(y) = \sqrt{\langle |\varepsilon_p(y)|^2 \rangle}$ and the gluon elliptic momentum anisotropy $v_2^g\{2\}(y) = \sqrt{\langle |v_2^g(y)|^2 \rangle}$ for the same centrality classes and parameter sets as in the eccentricities above. First, it is clear to see that both quantities follow each other closely. The anisotropy of the energy-momentum tensor is thus a good predictor of the gluon momentum anisotropy in the situation in which strong final state interactions are not included. Comparing the three panels, we can see that the initial momentum anisotropy increases with decreasing gluon multiplicity. The rapidity dependence of ε_p and v_2^g is negligible in most cases, with the case using $\alpha_s = 0.3$ (shown only for the most central bin) showing the strongest decrease with increasing rapidity. In the most peripheral bin the two quantities show a minimum around $y = 1$, which is where the transverse energy is maximal.

In Fig. 7 we focus on the centrality dependence of the rapidity dependent ε_2 , ε_3 , and v_2^g and compare results for the two different parameter sets $m = \tilde{m} = 0.2$ GeV and $m = \tilde{m} = 0.8$ GeV with $\alpha_s = 0.15$ in both cases.⁶ Generally, the sharper profiles for $m = \tilde{m} = 0.8$ GeV lead to larger geometric eccentricities ε_2 and ε_3 across all rapidities and centrality classes, as pointed out previously in [86]. While for $m = \tilde{m} = 0.8$ GeV both ε_2 and ε_3 exhibit a monotonic behavior as a function of centrality, we find that, for smaller values of the infrared regulator $m = \tilde{m} = 0.2$ GeV, the eccentricity ε_2 is maximal for 40%–50% central collisions and minimal in the most peripheral bin, and ε_3 increases monotonically toward more peripheral events and shows the strongest centrality dependence on the lead-going side.

On the other hand, the magnitude and centrality dependence of the gluon momentum anisotropy v_2^g is rather insensitive to the infrared regulator and only very weakly dependent on the rapidity. However, as has been observed previously [10,33], the initial momentum anisotropy driven v_2^g increases monotonically with decreasing multiplicity (toward more peripheral events). We show here that this is true for all studied rapidities. Furthermore, the value of v_2^g is largely independent of rapidity in all centrality bins, which is also a new result.

⁶Since ε_p and v_2^g are essentially identical, we show only the centrality dependence of v_2^g .

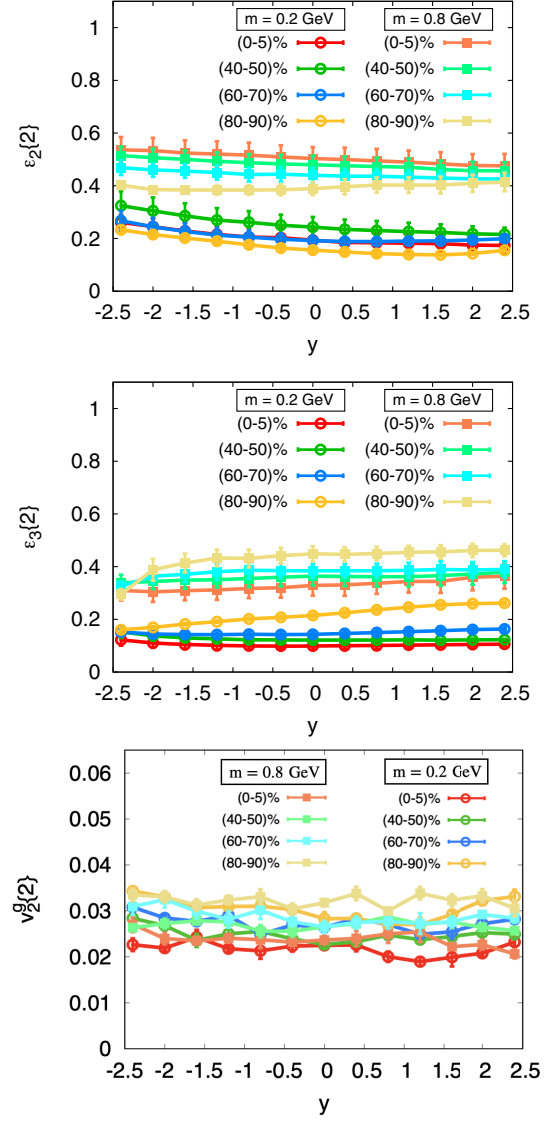


FIG. 7. Comparison of the rapidity dependence of $\sqrt{\langle |\varepsilon_2(y)|^2 \rangle}$ (top panel), $\sqrt{\langle |\varepsilon_3(y)|^2 \rangle}$ (middle panel), and $\sqrt{\langle |v_2^g(y)|^2 \rangle}$ (bottom panel) for different centrality classes for $\alpha_s = 0.15$ and distinct IR regulators such that $m = \tilde{m}$.

B. Decorrelation of event geometry and momentum anisotropy

Now that we have established the overall rapidity dependence of the initial state geometry and momentum anisotropy, we will investigate the correlation across different rapidities, as quantified by the correlation functions $C_{\varepsilon_2}(y_1, y_2)$ and $C_{\varepsilon_p}(y_1, y_2)$ shown in Fig. 8. The top panels show results for (0–5)% central collisions, the bottom panels for (60–70)% central collisions. The overall magnitude of this correlator is related to the size of ε_2 and ε_p , as $C_{\varepsilon_2}(y, y) = (\varepsilon_2\{2\}(y))^2$, and one proceeds similarly for C_{ε_p} . We see that $C_{\varepsilon_2}(y_1, y_2)$ is maximal for both rapidities being most negative, where the ε_2 is largest. Fixing one rapidity, we can see the decorrelation when varying the

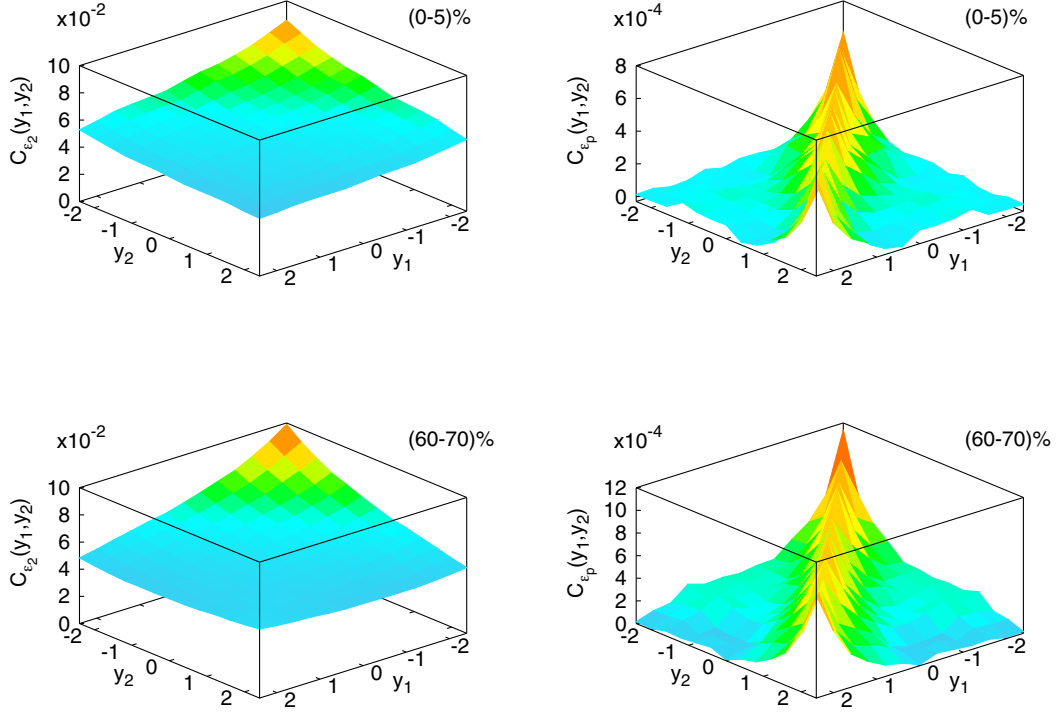


FIG. 8. Two-point correlation function for second order eccentricity ϵ_2 (top-left panel) and momentum anisotropy ϵ_p (top-right panel) for (0–5)% centrality class for $\alpha_s = 0.15$ and $m = 0.2$ GeV. The bottom panels demonstrate the same observable for (60–70)% centrality class.

other rapidity. $C_{\epsilon_p}(y_1, y_2)$ is maximal for $y_1 = y_2$ and does not vary much along this diagonal, as ϵ_p (or v_2^g) is approximately constant as a function of rapidity. However, when comparing the results for ϵ_2 and ϵ_p , we can already see that the decorrelation of the initial state momentum anisotropy in $C_{\epsilon_p}(y_1, y_2)$ is much faster than the decorrelation of the event geometry in $C_{\epsilon_2}(y_1, y_2)$. One also observes that $C_{\epsilon_2}(y_1, y_2)$ is only weakly dependent on centrality, while $C_{\epsilon_p}(y_1, y_2)$ shows some increase when going to more peripheral events, related to the increase of the initial state momentum anisotropy (v_2^g) for lower multiplicity.

In Fig. 9, we show the normalized correlation functions $C_{\epsilon_n}^N(\alpha_s \Delta y)$ for $n = 2, 3$, and $C_{v_2}^N(\alpha_s \Delta y)$ as functions of the scaled rapidity difference $\alpha_s \Delta y$. They are obtained from Eq. (22) as $C_{\mathcal{O}}^N(\Delta y) = \frac{1}{2y_{\max} - \Delta y} \int_{-y_{\max} + |\Delta y|/2}^{+y_{\max} - |\Delta y|/2} dY C_{\mathcal{O}}^N(Y + \Delta y/2, Y - \Delta y/2)$. For the geometric correlators we find that the decorrelation with rapidity is stronger for $n = 3$ than for $n = 2$. This is consistent with experimental observations in heavy ion collisions [87,88]. The decorrelation scales only approximately with α_s , as we see small differences between the $\alpha_s = 0.15$ and $\alpha_s = 0.3$ cases. As expected, smaller m leads to a faster decorrelation. The centrality dependence shown in the three top panels demonstrates how the rapidity decorrelation becomes faster toward more peripheral events.

In the bottom row of Fig. 9, we present the correlator for the gluon momentum anisotropy $C_{v_2}^N(\alpha_s \Delta y)$, which shows a much more rapid decorrelation than the geometric quantities but the opposite centrality dependence, with the most peripheral bin showing the broadest correlation in rapidity. The scaling with α_s works more accurately in this case, and smaller m leads only to a slightly faster decorrelation. The quick decorrelation in the initial momentum anisotropy with JIMWLK evolution compared to the geometric case can be expected based on the fact that every gluon emission in the evolution leads to a color decorrelation, quickly scrambling information of color domains at the initial rapidity. Conversely, the larger scale geometric structures are much more robust to the evolution, as they are not sensitive to the color structure.

The centrality dependence of these results is highlighted again in Fig. 10. For the geometric quantities, the width of the correlation function decreases with increasing centrality, while it increases for the initial momentum anisotropy. This can be understood as follows: The geometry of the more dilute peripheral events can be changed more easily by additional gluon emissions in the evolution (predominantly via the modification of the proton's shape). Denser protons are more robust to changes of the geometry by the same amount of emissions. Regarding the momentum anisotropy, it is maximal in the most peripheral bins. Consequently it takes more evolution to destroy it.

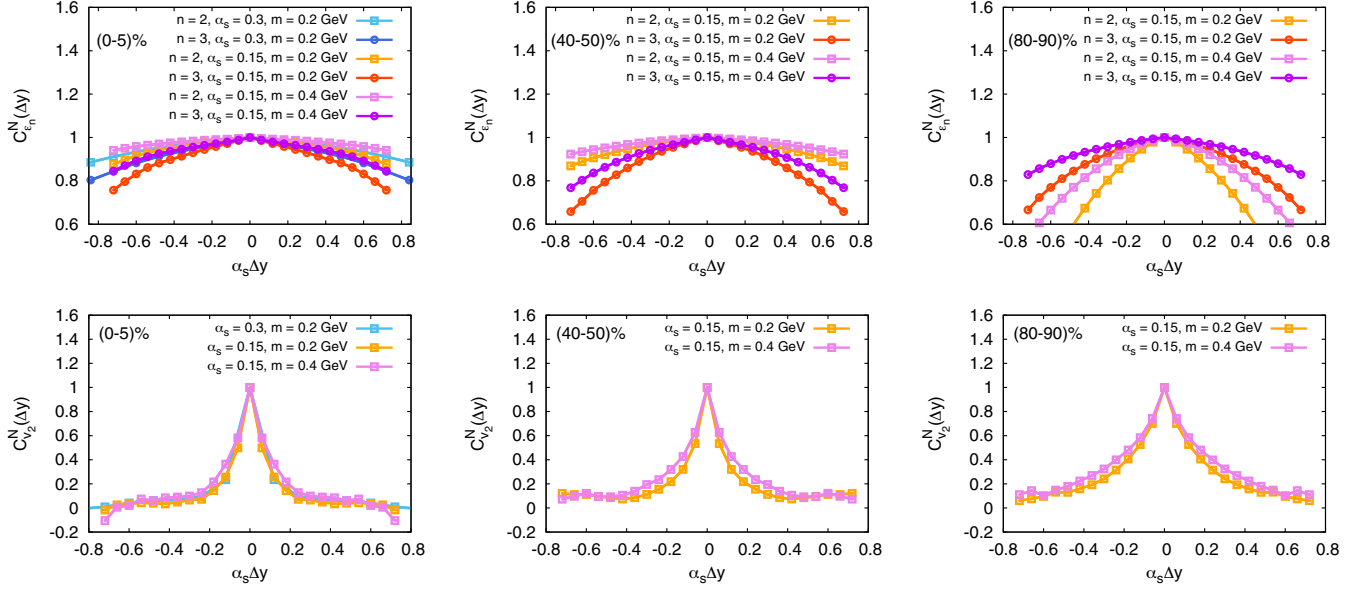


FIG. 9. Normalized two-point correlation functions $C^N(\Delta y)$ for geometric eccentricities $\varepsilon_2, \varepsilon_3$ (top row) and initial state momentum anisotropies v_2 (bottom row) for different centrality classes 0%–5% (left panels), 40%–50% (center panels), and 80%–90% (right panels) as a function of the rapidity separation $\alpha_s \Delta y$.

We find that in the most peripheral events, where the initial momentum anisotropy can potentially dominate the observed charged hadron anisotropy [57], the correlation drops by 50% within approximately one unit of rapidity (for the preferred JIMWLK evolution speed with $\alpha_s = 0.15$).

The two columns of Fig. 10 show the results for different choices of $m = \tilde{m}$. While we do see variations of the decorrelation speed with the choice of infrared regulator, particularly for the spatial anisotropy, our main conclusion that the initial momentum anisotropy decorrelates significantly more quickly than the geometry is robust.

In order to better understand the decorrelation that is observed in the event averaged quantities, we study both the real and imaginary parts of the spatial and momentum anisotropies for three individual events in Fig. 11. In the top row, we show the real and imaginary parts of ε_n as functions of rapidity. As expected from the slow decorrelation observed above, the plotted quantities vary smoothly and weakly with rapidity.

In the bottom row of Fig. 11, we show the real and imaginary parts of ε_p and v_2^g as functions of rapidity. For all events (the columns), we observe rather quick variations of the preferred direction of anisotropy with rapidity even though the magnitude of anisotropy given by the absolute value does not change too rapidly, even in a single event. These rapid variations explain the quick decrease of the correlator with rapidity, with the main driver being fluctuations in the angle. We note that, even in a single event, ε_p closely resembles v_2^g .

C. Estimators for the correlation between mean transverse momentum and elliptic anisotropy

Finally, we consider estimators for the correlation of mean transverse momentum and the elliptic anisotropy, which has been suggested as an observable to distinguish between geometry and initial momentum anisotropy as the origin of the observed anisotropy [57]. The relevant correlator studied experimentally is defined as

$$\hat{\rho}(v_2^2, [p_T]) = \frac{\langle \delta v_2^2 \delta [\hat{p}_T] \rangle}{\sqrt{\langle (\delta v_2^2)^2 \rangle \langle (\delta [\hat{p}_T])^2 \rangle}}, \quad (23)$$

where v_2 is the measured elliptic anisotropy and $[p_T]$ is the mean transverse momentum in a given event, and the event-by-event deviation for the observable O at fixed multiplicity is defined as [89]

$$\hat{\delta}O \equiv \delta O - \frac{\langle \delta O \delta N \rangle}{\sigma_N^2} \delta N, \quad (24)$$

where $\delta O = O - \langle O \rangle$, N is the multiplicity, and σ_N is the variance of N in a given centrality bin.

Because we are considering initial state quantities in this work, we compute estimators for $\hat{\rho}$ by replacing v_2 with ε_2 (or ε_p) and replacing $[p_T]$ with the average entropy density $[s] = [e^{3/4}]$, where e is the energy density, approximated as $T^{\tau\tau}$. The average $[f]$ is computed as

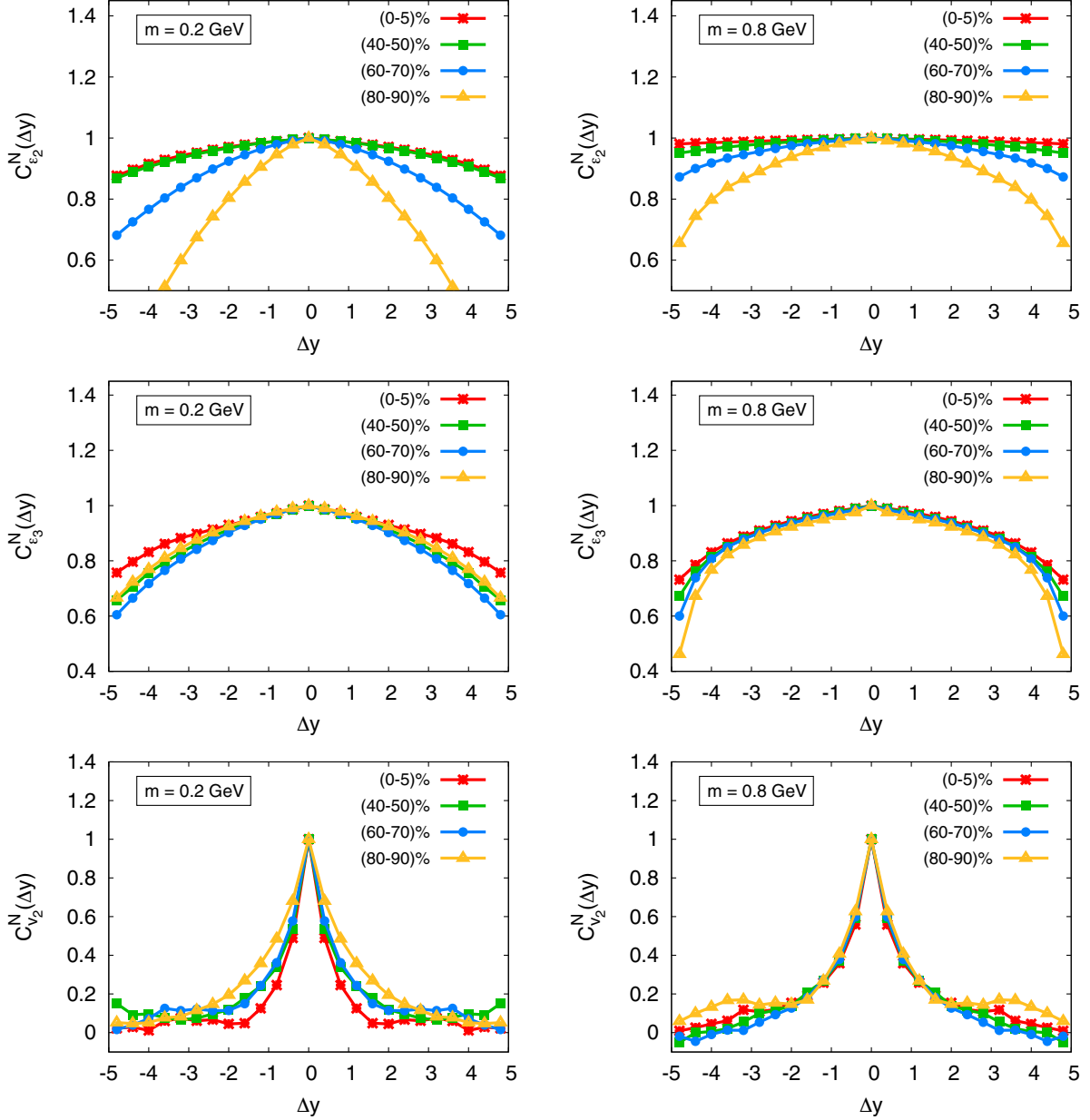


FIG. 10. Comparison of the normalized correlation function $C_O^N(\Delta y)$ of the geometric eccentricity ϵ_2 (top panels), ϵ_3 (middle panels), and initial state gluon momentum anisotropy v_2 (bottom panels) for different centrality classes using $\alpha_s = 0.15$ and $m = \tilde{m} = 0.2$ GeV (left panels) or 0.8 GeV (right panels).

$$[f] = \frac{\int d^2\mathbf{x}_\perp e(\mathbf{x}_\perp) f(\mathbf{x}_\perp)}{\int d^2\mathbf{x}_\perp e(\mathbf{x}_\perp)}. \quad (25)$$

The estimator using the ellipticity ϵ_2 , $\hat{\rho}_{\text{est}}(\epsilon_2^2, [s])$, is shown as a function of centrality in the top panel of Fig. 12 for two different ways of choosing the rapidity bins where the different components of $\hat{\rho}$ are computed. One takes all quantities at rapidity zero ($y = 0$), while the other uses three different rapidity bins (the ABC regions) for the different components of $\hat{\rho}$, following the prescription used by the ATLAS Collaboration [90]. We find that for the larger $m = \tilde{m}$ the geometry estimator is always negative, as

can be expected from geometric considerations [57]. Since the infrared regulators m, \tilde{m} have a strong effect on the event geometry, this also affects the $\hat{\rho}$ estimator. When considering the smaller $m = \tilde{m}$, we even find positive values for most central and most peripheral events. While this is at odds with calculations of this estimator in the IP-Glasma model without JIMWLK evolution [57], it is conceivable that the JIMWLK evolution, which has greater effects on the geometry for smaller m , causes this difference in the most central and most peripheral events. The appearance of positive values for smaller m , which leads to larger systems, is in line with findings in a previous

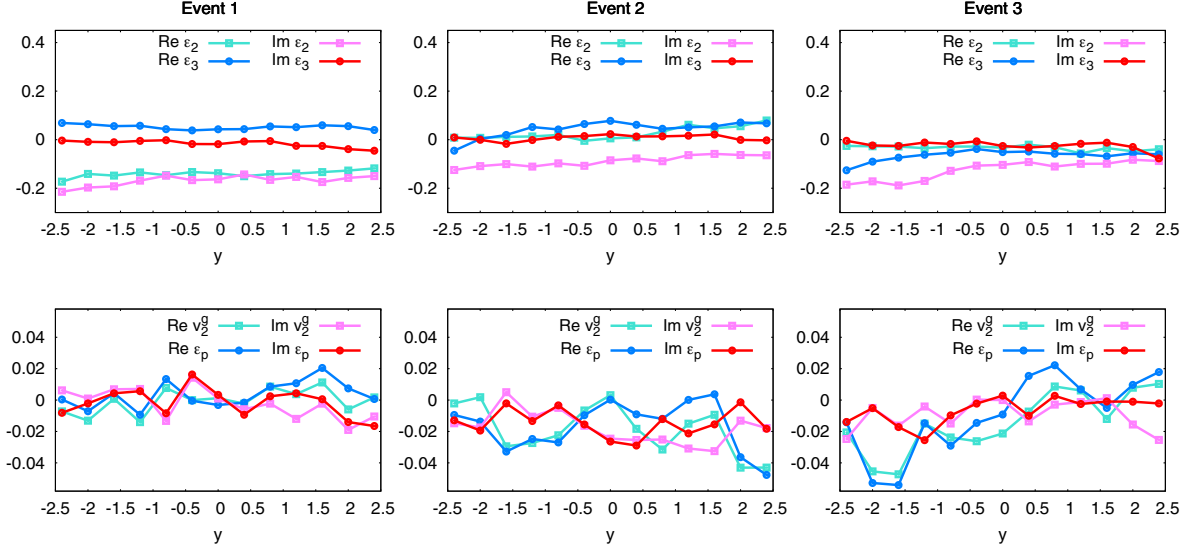


FIG. 11. Rapidity dependence of the real and imaginary parts of the second and third order spatial eccentricities (top row) for three different events in the (0–5)% centrality class (top row). Similar results are given for the azimuthal anisotropy of initial state gluon v_2^g and initial state momentum anisotropy ϵ_p in the bottom row. The simulation parameters are $\alpha_s = 0.15$ and $m = \tilde{m} = 0.2$ GeV.

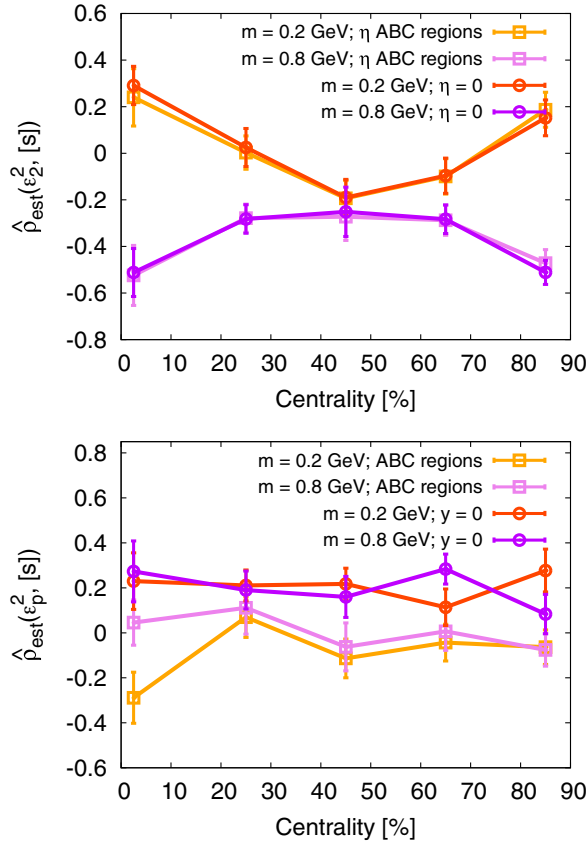


FIG. 12. Estimators based on the initial geometry $\hat{\rho}_{\text{est}}(\epsilon_2^2, [s])$ (top panel) and initial state momentum anisotropy $\hat{\rho}_{\text{est}}(\epsilon_p^2, [s])$ (bottom panel) as a function of centrality for two different values of the infrared regulator ($m = \tilde{m}$). The correlation measure denoted as ABC is obtained for different rapidity regions: region A with $-2.4 < y < -0.8$, central region B with $|y| < 0.8$, and region C with $0.8 < y < 2.4$.

work, where the geometric $\hat{\rho}$ correlator turned positive when increasing the system size [91].

Most importantly, for the geometric estimator, we do not see a large dependence on the choice of rapidity bins, which is related to the weak decorrelation of the geometry observed. Hence, our results justify the use of the boost-invariant approximation to compute the correlator in geometry driven models [57,91].

When replacing ϵ_2 by the initial state momentum anisotropy ϵ_p , we observe a positive correlation in the $\hat{\rho}_{\text{est}}(\epsilon_p^2, [s])$ estimator while considering both quantities at midrapidity, which again is in line with the findings in [57]. However, owing to the rapid decorrelation of ϵ_p in rapidity, this signal does not appear to survive the rapidity gap, as the correlator $\hat{\rho}_{\text{est}}(\epsilon_p^2, [s])$ is consistent with zero when one considers the selection in different rapidity intervals (ABC).

V. CONCLUSIONS AND OUTLOOK

We presented results for rapidity dependent quantities in $p + \text{Pb}$ collisions, computed within the color glass condensate framework, which involves the calculation of classical gluon fields in the proton and lead nucleus in IP-Glasma, their leading quantum corrections via JIMWLK evolution of the corresponding Wilson lines, and computation of production and time evolution of the gluon fields generated by the collision at different rapidities. We showed results for the rapidity dependence of gluon production dN_g/dy and the transverse energy dE_\perp/dy for different centralities, and we analyzed the role of the saturation scale Q_s in the proton and nucleus, as well as that of the overlapping area for gluon production as a function of centrality.

We studied the transverse geometry, quantified by the eccentricities ε_2 and ε_3 as a function of centrality and rapidity, finding rather mild dependencies. The initial momentum anisotropy, quantified by either the anisotropy of the energy-momentum tensor ε_p or that of the gluon distribution v_2^g , showed a weak rapidity dependence for all centralities and increased when centrality from central to peripheral events increased.

We computed the unequal rapidity correlations of both the geometric and initial momentum anisotropy vectors and observed very different behavior between the two. The geometry decorrelates much more slowly as a function of the rapidity difference than in the initial momentum anisotropy. In the latter, the correlation is widest in the most peripheral centrality bin but still drops to about half its maximal value for a rapidity difference $\Delta y = 1$. This result implies that, when using large rapidity gaps to measure flow harmonics or the $\hat{\rho}$ correlator experimentally, the initial momentum anisotropy may play a smaller role than previously assumed. In order to access this contribution, smaller rapidity gaps need to be employed, which will make the separation from other nonflow effects difficult.

Regarding the geometry, we find a faster decorrelation for ε_3 than for ε_2 , which is in line with observations in heavy ion collisions [87,88]. The fast decorrelation of ε_3 can play an important role in the difference between different v_3 measurements in small asymmetric systems at RHIC [56,92–94].

For all these observables, we studied in detail the dependence on the infrared regulators employed in the calculation, as well as that on the strong coupling constant α_s , which controls the evolution speed of the JIMWLK equations. We assumed a fixed coupling constant. Running coupling effects have been included in leading logarithmic JIMWLK evolution calculations [78,95,96]. Generally, their inclusion should lead to a faster rapidity evolution of the long-range geometric structures, and a slower evolution of short-range momentum correlations in the transverse plane.

Finally, we computed an initial state estimator for the correlation between the elliptic anisotropy and the average transverse momentum at fixed multiplicity. For the larger infrared regulator, this quantity is always negative, which is in line with previous findings using the IP-Glasma model (without JIMWLK evolution) [57]. For the smaller regulator, positive values are found in the most central and most peripheral bins, which could be attributed to effects from the JIMWLK evolution on the details of the geometry at large length scales.

We conclude that even at collision energies available at the LHC, for small systems the rapidity dependence is not to be neglected. When rapidity gaps are employed experimentally, the theoretical description will not get away with the assumption of boost invariance in most cases. Rapidity dependent calculations are required and the experimental

procedures should be matched as closely as possible. Even the centrality selection is already affected by the rapidity dependence, and we recommend that—for the purpose of an easier comparison to theoretical calculations—future experimental studies perform their centrality selection around mid-rapidity.

We note that, from a theoretical point of view, our description calculates mean-field type correlations and propagates them using JIMWLK evolution. The subleading correction to the limit of a large number of small- x constituents includes the absence of particles that had already scattered and conditional constraints on the small- x evolution. We are not aware of how to include these effects in dense-dense calculations, and their potential effects on the observables studied are unclear. However, by considering the dilute limit of the projectile, Iancu and Triantafyllopoulos [97,98] developed a framework to study multiparticle production with rapidity correlations, which may provide a way to assess these effects in future studies.

In the future, it will also be interesting to couple the computed rapidity dependent initial state to hydrodynamics, possibly via an intermediate kinetic theory stage [99,100]. Also, a construction of a fully three-dimensional Wilson line configuration followed by $3 + 1$ D Yang-Mills evolution, as explored in [101–103], will be desirable.

ACKNOWLEDGMENTS

S.S. and P.S. are supported by the Deutsche Forschungsgemeinschaft (DFG, German Research Foundation) through the CRC-TR 211 “Strong Interaction Matter under Extreme Conditions”—Project No. 315477589–TRR 211. P.S. is also supported by the Academy of Finland under Project No. 321840 and under the European Union’s Horizon 2020 research and innovation program by the STRONG-2020 project (Grant Agreement No. 824093). B.S. is supported by the U.S. Department of Energy, Office of Science, Office of Nuclear Physics, under Contract No. DE-SC0012704. This research used the resources of the National Energy Research Scientific Computing Center, a DOE Office of Science User Facility supported by the Office of Science of the U.S. Department of Energy under Contract No. DE-AC02-05CH11231.

APPENDIX: DIPOLE AMPLITUDE AND SATURATION SCALE

In order to characterize the gluon distribution of the proton and the Pb nucleus, we use the dipole scattering amplitude, Eq. (15), where $\mathbf{d}_\perp = (\mathbf{x}_\perp + \mathbf{y}_\perp)/2$ is the impact parameter and $\mathbf{r}_\perp = \mathbf{x}_\perp - \mathbf{y}_\perp$ is the size of a color singlet dipole with color charges at positions \mathbf{x}_\perp and \mathbf{y}_\perp . We show the dipole scattering amplitude $1 - D(\mathbf{r}_\perp, |\mathbf{d}_\perp| < 0.2R_p)$ for the Pb nucleus (top row) and proton (bottom row) as a function of dipole size $r_\perp = |\mathbf{r}_\perp|$ for a fixed range of impact parameter $|\mathbf{d}_\perp| < 0.2R_p$ measured at three different rapidities

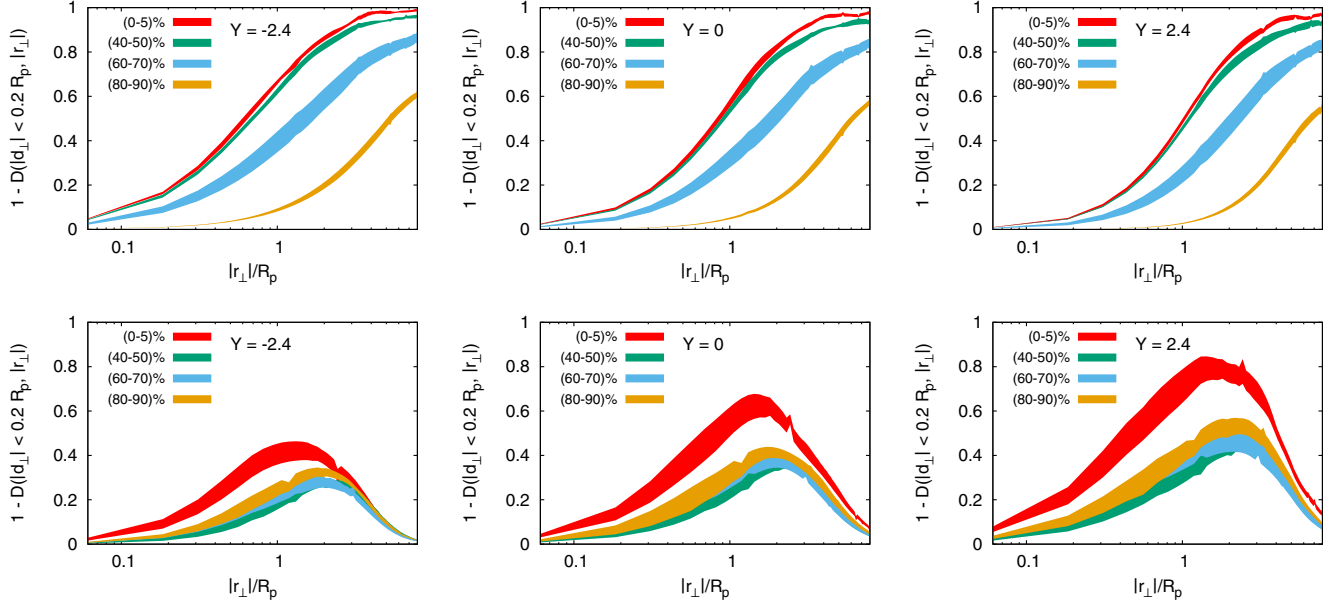


FIG. 13. Dipole scattering amplitudes $1 - D(\mathbf{r}_\perp, |\mathbf{d}_\perp| < 0.2 R_p)$ of the lead nucleus (top row) and proton (bottom row) at three different rapidities $Y = -2.4, 0, +2.4$ as a function of dipole size $|\mathbf{r}_\perp|$ in units of the proton radius R_p .

$y = -2.4, 0, +2.4$ in various centrality classes in Fig. 13. This choice of \mathbf{d}_\perp is based on [79], where the dominant support of $D(|\mathbf{d}_\perp|, |\mathbf{r}_\perp|)$ dwells in the region of the small impact parameter.

Owing to the color transparency the dipole scattering amplitude $1 - D$ vanishes at $r_\perp = 0$ and then gradually rises and reaches a maximum at $r_\perp/R_p \sim 1$. For the Pb nucleus we observe that the scattering amplitude saturates for the (0–5)% and (40–50)% centrality classes, while the other two centrality classes are dilute even for $Y = -2.4$, which corresponds to the smallest x . For proton (bottom row of Fig. 13), the dipole amplitude is significantly below the saturation level, even after a full rapidity evolution ($Y = 2.4$), and starts to fall when the separation between the dipole exceeds the size of the proton ($r_\perp \gg R_p$) because the dipole no longer hits the target, as previously observed in [79]. We also note that for protons the shape of the dipole amplitude as a function of r_\perp does not change much with centrality, particularly for the three more peripheral bins.

In order to investigate the system size, we use the Weizsäcker-Williams fields E_μ^- , which are represented by lightlike Wilson lines $V_{p/Pb}$ on a two-dimensional lattice with transverse coordinates as

$$E_{j,x}^- = \frac{i}{4} [V_{x+j}^\dagger V_x + V_x^\dagger V_{x-j} - V_x^\dagger V_{x+j} - V_{x-j}^\dagger V_x] - \frac{i}{4N_c} \text{Tr} [V_{x+j}^\dagger V_x + V_x^\dagger V_{x-j} - V_x^\dagger V_{x+j} - V_{x-j}^\dagger V_x]. \quad (\text{A1})$$

The mean radius squared is then determined from $E^2(\mathbf{x}_\perp) = \text{Tr}[E_x^-(\mathbf{x}_\perp)E_x^-(\mathbf{x}_\perp) + E_y^-(\mathbf{x}_\perp)E_y^-(\mathbf{x}_\perp)]$ as

$$\langle r_\perp^2(y) \rangle = \frac{\int d^2 \mathbf{r}_\perp \mathbf{r}_\perp^2 E^2(\mathbf{r}_\perp, y)}{\int d^2 \mathbf{r}_\perp E^2(\mathbf{r}_\perp, y)}, \quad (\text{A2})$$

Similarly, the transverse area S_\perp is obtained as

$$S_\perp = \int \Theta(E^2(\mathbf{x}_\perp) - \Lambda^2) d^2 \mathbf{x}_\perp, \quad (\text{A3})$$

where the Heaviside function implies that only regions with field strength $E^2(\mathbf{x}_\perp)$ larger than the cutoff scale $\Lambda^2 = 0.02 \text{ GeV/fm}^3$ contribute to the integral. The results for $\langle r_\perp^2 \rangle$ and S_\perp as a function of rapidity for different centrality classes for proton (left panels) and Pb nucleus (right panels) are summarized in Fig. 14. We find that, as in Fig. 5, the mean radius squared grows almost linearly in the direction of increasing (decreasing) rapidity for the proton (Pb nucleus) and is considerably independent of centrality, except for the most central bin being different from the other three.

We observe that for the left moving proton the transverse area S_\perp grows quadratically with decreasing x , which is in agreement with the observation made in [79], where the similarly defined proton radius grows linearly with the rapidity evolution. Since the transverse size S_\perp of the Pb nucleus is significantly larger to begin with, the effect of Gribov diffusion on the Pb nucleus is smaller, leading to a slower increase of the area with decreasing x (decreasing rapidity). With regard to the centrality dependence, one finds that due to the larger overall field strength the transverse area S_\perp of protons is somewhat larger for the most central events, while for the Pb nucleus no significant centrality dependence is observed.

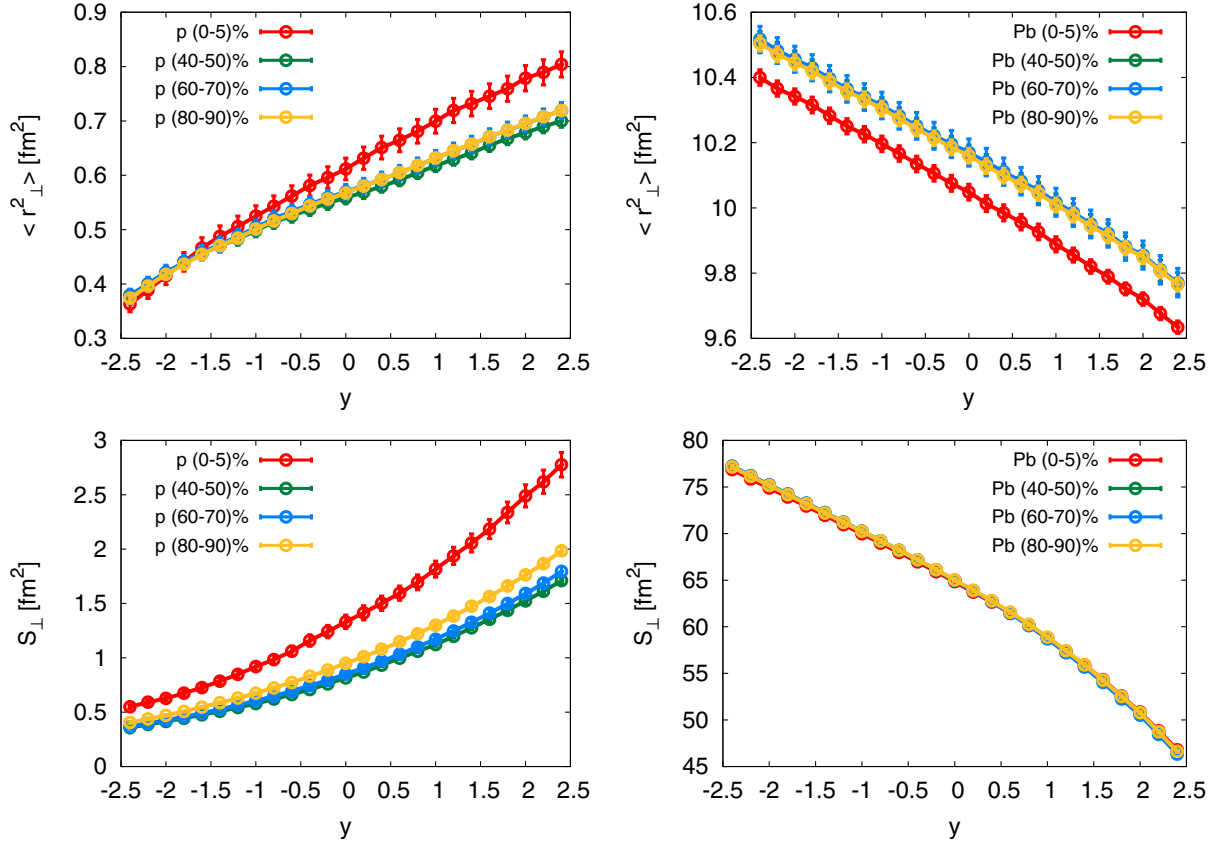


FIG. 14. Mean radius squared (top row) and transverse area (bottom row) for proton (left column) and Pb nucleus (right column) as a function of rapidity for different centrality classes. Simulation parameter: $\alpha_s = 0.15$ and $m = \bar{m} = 0.2$ GeV.

-
- [1] D. A. Teaney, in *Quark-Gluon Plasma 4*, edited by R. C. Hwa and X.-N. Wang (World Scientific, Singapore, 2010), pp. 207–266.
- [2] C. Gale, S. Jeon, and B. Schenke, *Int. J. Mod. Phys. A* **28**, 1340011 (2013).
- [3] M. Luzum and H. Petersen, *J. Phys. G* **41**, 063102 (2014).
- [4] U. Heinz and R. Snellings, *Annu. Rev. Nucl. Part. Sci.* **63**, 123 (2013).
- [5] S. Jeon and U. Heinz, *Int. J. Mod. Phys. E* **24**, 1530010 (2015).
- [6] K. Dusling, W. Li, and B. Schenke, *Int. J. Mod. Phys. E* **25**, 1630002 (2016).
- [7] C. Loizides, *Nucl. Phys. A* **956**, 200 (2016).
- [8] S. Schlichting and P. Tribedy, *Adv. High Energy Phys.* (2016) 8460349.
- [9] J. L. Nagle and W. A. Zajc, *Annu. Rev. Nucl. Part. Sci.* **68**, 211 (2018).
- [10] B. Schenke, C. Shen, and P. Tribedy, *Phys. Lett. B* **803**, 135322 (2020).
- [11] B. Schenke, *Rep. Prog. Phys.* **84**, 082301 (2021).
- [12] G. Aad *et al.* (ATLAS Collaboration), *Phys. Rev. C* **104**, 014903 (2021).
- [13] W. Florkowski, M. P. Heller, and M. Spalinski, *Rep. Prog. Phys.* **81**, 046001 (2018).
- [14] L. He, T. Edmonds, Z.-W. Lin, F. Liu, D. Molnar, and F. Wang, *Phys. Lett. B* **753**, 506 (2016).
- [15] M. Greif, C. Greiner, B. Schenke, S. Schlichting, and Z. Xu, *Phys. Rev. D* **96**, 091504 (2017).
- [16] P. Romatschke, *Eur. Phys. J. C* **78**, 636 (2018).
- [17] P. P. Bhaduri, N. Borghini, A. Jaiswal, and M. Strickland, *Phys. Rev. C* **100**, 051901 (2019).
- [18] N. Kersting, N. Borghini, and S. Feld, *MDPI Proc.* **10**, 16 (2019).
- [19] H. Roch and N. Borghini, *Eur. Phys. J. C* **81**, 380 (2021).
- [20] A. Kurkela, U. A. Wiedemann, and B. Wu, *Eur. Phys. J. C* **79**, 759 (2019).
- [21] A. Kurkela, U. A. Wiedemann, and B. Wu, *Eur. Phys. J. C* **79**, 965 (2019).
- [22] A. Kurkela, S. F. Taghavi, U. A. Wiedemann, and B. Wu, *Phys. Lett. B* **811**, 135901 (2020).

- [23] A. Dumitru, F. Gelis, L. McLerran, and R. Venugopalan, *Nucl. Phys.* **A810**, 91 (2008).
- [24] A. Kovner and M. Lublinsky, *Phys. Rev. D* **83**, 034017 (2011).
- [25] A. Dumitru, K. Dusling, F. Gelis, J. Jalilian-Marian, T. Lappi, and R. Venugopalan, *Phys. Lett. B* **697**, 21 (2011).
- [26] A. Kovner and M. Lublinsky, *Phys. Rev. D* **84**, 094011 (2011).
- [27] K. Dusling and R. Venugopalan, *Phys. Rev. Lett.* **108**, 262001 (2012).
- [28] E. Levin and A. H. Rezaeian, *Phys. Rev. D* **84**, 034031 (2011).
- [29] K. Dusling and R. Venugopalan, *Phys. Rev. D* **87**, 054014 (2013).
- [30] K. Dusling and R. Venugopalan, *Phys. Rev. D* **87**, 094034 (2013).
- [31] A. Dumitru and A. V. Giannini, *Nucl. Phys.* **A933**, 212 (2015).
- [32] A. Dumitru, L. McLerran, and V. Skokov, *Phys. Lett. B* **743**, 134 (2015).
- [33] B. Schenke, S. Schlichting, and R. Venugopalan, *Phys. Lett. B* **747**, 76 (2015).
- [34] L. McLerran and V. Skokov, *Nucl. Phys.* **A947**, 142 (2016).
- [35] B. Schenke, S. Schlichting, P. Tribedy, and R. Venugopalan, *Phys. Rev. Lett.* **117**, 162301 (2016).
- [36] K. Dusling, M. Mace, and R. Venugopalan, *Phys. Rev. Lett.* **120**, 042002 (2018).
- [37] K. Dusling, M. Mace, and R. Venugopalan, *Phys. Rev. D* **97**, 016014 (2018).
- [38] M. Mace, V. V. Skokov, P. Tribedy, and R. Venugopalan, *Phys. Rev. Lett.* **121**, 052301 (2018); **123**, 039901(E) (2019).
- [39] M. Mace, V. V. Skokov, P. Tribedy, and R. Venugopalan, *Phys. Lett. B* **788**, 161 (2019); **799**, 135006(E) (2019).
- [40] A. Kovner and V. V. Skokov, *Phys. Lett. B* **785**, 372 (2018).
- [41] P. Bozek, *Phys. Rev. C* **85**, 014911 (2012).
- [42] P. Bozek and W. Broniowski, *Phys. Lett. B* **718**, 1557 (2013).
- [43] P. Bozek and W. Broniowski, *Phys. Lett. B* **720**, 250 (2013).
- [44] P. Bozek and W. Broniowski, *Phys. Rev. C* **88**, 014903 (2013).
- [45] P. Bozek, W. Broniowski, and G. Torrieri, *Phys. Rev. Lett.* **111**, 172303 (2013).
- [46] A. Bzdak, B. Schenke, P. Tribedy, and R. Venugopalan, *Phys. Rev. C* **87**, 064906 (2013).
- [47] G.-Y. Qin and B. Müller, *Phys. Rev. C* **89**, 044902 (2014).
- [48] K. Werner, M. Bleicher, B. Guiot, I. Karpenko, and T. Pierog, *Phys. Rev. Lett.* **112**, 232301 (2014).
- [49] I. Kozlov, M. Luzum, G. Denicol, S. Jeon, and C. Gale, *arXiv:1405.3976*.
- [50] B. Schenke and R. Venugopalan, *Phys. Rev. Lett.* **113**, 102301 (2014).
- [51] P. Romatschke, *Eur. Phys. J. C* **75**, 305 (2015).
- [52] C. Shen, J.-F. Paquet, G. S. Denicol, S. Jeon, and C. Gale, *Phys. Rev. C* **95**, 014906 (2017).
- [53] R. D. Weller and P. Romatschke, *Phys. Lett. B* **774**, 351 (2017).
- [54] H. Mäntysaari, B. Schenke, C. Shen, and P. Tribedy, *Phys. Lett. B* **772**, 681 (2017).
- [55] B. Schenke, C. Shen, and P. Tribedy, *Phys. Rev. C* **102**, 044905 (2020).
- [56] J. L. Nagle, R. Belmont, S. H. Lim, and B. Seidlitz, *Phys. Rev. C* **105**, 024906 (2022).
- [57] G. Giacalone, B. Schenke, and C. Shen, *Phys. Rev. Lett.* **125**, 192301 (2020).
- [58] B. Schenke and S. Schlichting, *Phys. Rev. C* **94**, 044907 (2016).
- [59] F. Gelis, T. Lappi, and R. Venugopalan, *Phys. Rev. D* **78**, 054019 (2008).
- [60] F. Gelis, T. Lappi, and R. Venugopalan, *Phys. Rev. D* **78**, 054020 (2008).
- [61] E. Iancu and R. Venugopalan, in *Quark-Gluon Plasma 4*, edited by R. C. Hwa and X.-N. Wang (World Scientific, Singapore, 2003), pp. 249–363.
- [62] B. Schenke, P. Tribedy, and R. Venugopalan, *Phys. Rev. Lett.* **108**, 252301 (2012).
- [63] B. Schenke, P. Tribedy, and R. Venugopalan, *Phys. Rev. C* **86**, 034908 (2012).
- [64] J. Jalilian-Marian, A. Kovner, L. D. McLerran, and H. Weigert, *Phys. Rev. D* **55**, 5414 (1997).
- [65] J. Jalilian-Marian, A. Kovner, A. Leonidov, and H. Weigert, *Nucl. Phys.* **B504**, 415 (1997).
- [66] J. Jalilian-Marian, A. Kovner, A. Leonidov, and H. Weigert, *Phys. Rev. D* **59**, 014014 (1998).
- [67] E. Iancu, A. Leonidov, and L. D. McLerran, *Nucl. Phys.* **A692**, 583 (2001).
- [68] E. Iancu, A. Leonidov, and L. D. McLerran, *Phys. Lett. B* **510**, 133 (2001).
- [69] L. D. McLerran and R. Venugopalan, *Phys. Rev. D* **49**, 3352 (1994).
- [70] L. D. McLerran and R. Venugopalan, *Phys. Rev. D* **50**, 2225 (1994).
- [71] T. Lappi, *Eur. Phys. J. C* **55**, 285 (2008).
- [72] J. Bartels, K. J. Golec-Biernat, and H. Kowalski, *Phys. Rev. D* **66**, 014001 (2002).
- [73] H. Kowalski and D. Teaney, *Phys. Rev. D* **68**, 114005 (2003).
- [74] A. H. Rezaeian, M. Siddikov, M. Van de Klundert, and R. Venugopalan, *Phys. Rev. D* **87**, 034002 (2013).
- [75] B. Schenke and C. Shen, The official code repository of the IP-Glasma initial conditions can be found at <https://github.com/schenke/ipglasma>. Here we used v1.0: <https://github.com/schenke/ipglasma/releases/tag/1.0>.
- [76] H. Weigert, *Nucl. Phys.* **A703**, 823 (2002).
- [77] J.-P. Blaizot, E. Iancu, and H. Weigert, *Nucl. Phys.* **A713**, 441 (2003).
- [78] T. Lappi and H. Mäntysaari, *Eur. Phys. J. C* **73**, 2307 (2013).
- [79] S. Schlichting and B. Schenke, *Phys. Lett. B* **739**, 313 (2014).
- [80] A. Kovner and U. A. Wiedemann, *Phys. Rev. D* **66**, 051502 (2002).
- [81] A. Krasnitz and R. Venugopalan, *Nucl. Phys.* **B557**, 237 (1999).

- [82] S. Chatrchyan *et al.* (CMS Collaboration), *Phys. Lett. B* **718**, 795 (2013).
- [83] J. Adam *et al.* (ALICE Collaboration), *Phys. Rev. C* **91**, 064905 (2015).
- [84] A. Dumitru and L. D. McLerran, *Nucl. Phys. A* **700**, 492 (2002).
- [85] T. Lappi, *Phys. Lett. B* **643**, 11 (2006).
- [86] S. Demirci, T. Lappi, and S. Schlichting, *Phys. Rev. D* **103**, 094025 (2021).
- [87] V. Khachatryan *et al.* (CMS Collaboration), *Phys. Rev. C* **92**, 034911 (2015).
- [88] G. Aad *et al.* (ATLAS Collaboration), *Phys. Rev. Lett.* **126**, 122301 (2021).
- [89] A. Olszewski and W. Broniowski, *Phys. Rev. C* **96**, 054903 (2017).
- [90] G. Aad *et al.* (ATLAS Collaboration), *Eur. Phys. J. C* **79**, 985 (2019).
- [91] P. Bozek and H. Mehrabpour, *Phys. Rev. C* **101**, 064902 (2020).
- [92] C. Aidala *et al.* (PHENIX Collaboration), *Nat. Phys.* **15**, 214 (2019).
- [93] R. A. Lacey (STAR Collaboration), *Nucl. Phys. A* **1005**, 122041 (2021).
- [94] U. A. Acharya *et al.* (PHENIX Collaboration), *Phys. Rev. C* **105**, 024901 (2022).
- [95] T. Lappi, *Phys. Lett. B* **703**, 325 (2011).
- [96] A. Dumitru, J. Jalilian-Marian, T. Lappi, B. Schenke, and R. Venugopalan, *Phys. Lett. B* **706**, 219 (2011).
- [97] E. Iancu and D. N. Triantafyllopoulos, *J. High Energy Phys.* **11** (2013) 067.
- [98] E. Iancu and D. N. Triantafyllopoulos, *Nucl. Phys. A* **926**, 166 (2014).
- [99] A. Kurkela, A. Mazeliauskas, J.-F. Paquet, S. Schlichting, and D. Teaney, *Phys. Rev. C* **99**, 034910 (2019).
- [100] A. Kurkela, A. Mazeliauskas, J.-F. Paquet, S. Schlichting, and D. Teaney, *Phys. Rev. Lett.* **122**, 122302 (2019).
- [101] S. McDonald, S. Jeon, and C. Gale, *Nucl. Phys. A* **1005**, 121771 (2021).
- [102] S. Schlichting and P. Singh, *Phys. Rev. D* **103**, 014003 (2021).
- [103] A. Ipp, D. I. Müller, S. Schlichting, and P. Singh, *Phys. Rev. D* **104**, 114040 (2021).